Polymer-assisted deposition of $SrRuO_3$ thin films

Maarten Nijland

Student number: s0089966

Graduate committee: Prof. dr. ing. D.H.A. Blank (chair)
Dr. O.F. Göbel (tutor)
Dr. A.J.A. Winnubst (member from other research group)
Dr. ir. J.E. ten Elshof
Dr. ir. G. Koster

Date: May 15, 2010

Place: Enschede, the Netherlands

Description: Master's thesis Chemical Engineering, University of Twente

Version: Final

"Anything you build on a large scale or with intense passion invites chaos."

Francis Ford Coppola; 1998

American film director, producer and screenwriter

Abstract

Polymer-assisted deposition was introduced as a viable technique to create all sorts of metal oxide thin films. The technique was illustrated to profit from the advantages associated with current chemical solution deposition techniques. At the same time, polymer-assisted deposition was described to remove major drawbacks conventionally associated with this class of deposition methods. Most of these conclusions were based on studies of epitaxial film growth. The applicability of polymer-assisted deposition to form non-epitaxial films had so far not been extensively studied. The formation of polycrystalline $SrRuO_3$ thin films on substrates that could not act as a template during growth, was attempted in this work.

Stable polymeric solutions were made containing strontium and ruthenium precursor complexes. These solutions were spin cast and annealed, particularly on oxidized silicon substrates. A standard procedure was developed to create thin films from the solutions. Deviations were made to the procedure in order to gain a better understanding of the film forming processes. The goal of these experiments was to ultimately find a route that could lead to smooth and dense conductive thin films of $SrRuO_3$.

The films that resulted from the standard procedure contained protruding parts, that had developed during the thermal treatment. Protrusions of different shape and composition were found on films annealed at $600\,^{\circ}\mathrm{C}$ and $850\,^{\circ}\mathrm{C}$. X-ray diffraction studies indicated the presence of $SrRuO_3$ in the former case, but did not provide evidence for presence of any phase in the latter case. The various attempts that were made to inhibit the formation of these protrusions and simultaneously create thin films of proper density, composition, and crystallinity, did not have the desired effect.

Protrusions are believed to form by nucleation of $SrRuO_3$ crystallites at the substrate surface. The growth of these crystallites is expected to be facilitated by large diffusion lengths in the film, that are the result of simultaneously occurring decomposition events that reduce the film viscosity. The high curvature that these protrusions possess may explain why the crystallites were found unstable at processing temperatures of $850\,^{\circ}\mathrm{C}$. The results from the various attempts to improve the thin films, demonstrate the challenge to create $SrRuO_3$ thin films on substrates that can not act as template for epitaxial growth (*e.g.* amorphous substrates).

Table of contents

List of figures and tables

Figures

Tables

Preface

Starting a Master's thesis with a quotation of a film director is unarguably not the most straightforward decision to make. After all, the fields of materials science and movie production seem light-years away from each other. Nevertheless, the past few months which I spent working on polymer-assisted deposition, the large gap between both fields seemed to narrow. In my many attempts to understand and control film formation processes, I constantly concentrated on the ultimate goal to create 'high quality films'. A similar description will fit the work of a film director.

Soon after this project started, I was confronted with the chaos that developed in the films. I was determined to improve the film forming process to ultimately find a low cost method to efficiently create $SrRuO_3$ films preferably on low cost substrates. I soon realized that this was a challenging goal.

As I like to be challenged, I carried out all sorts of experiments that I thought could contribute to the quality of the films. I began to feel confident with the topic and tried to proceed systematically. During the last experiments, I discovered that the theory that I had developed contained an essential error. Although I still regret this error, it made me learn that I should work even more systematically, take more time to communicate with others about my work and always should try to avoid making any assumptions.

With the words on the first page, Francis Ford Coppola tried to say that true satisfaction will not be achieved without striking a blow. Although I had certainly be more satisfied if I had developed a viable alternative to the production of $SrRuO_3$ thin films, I am very content with the knowledge I gained during the past year. Besides, I think that the results that are covered in this report may contribute to a further understanding of the formation of $SrRuO_3$ and the applicability of polymer-assisted deposition.

Enschede; May 12, 2010

Maarten Nijland

Introduction

Conductivity is to metals as insulation is to oxides. These words could almost be the answer to a question in a typical IQ test. Almost, because not all oxide materials are insulators. The exceptions can not be found in common oxides like clay or glass, but are found in more 'advanced materials'. An example of such a material is $SrRuO_3$ (strontium ruthenate or SRO in short).

SRO is a metallic conducting oxide with a room temperature resistivity of $280\ \mu\Omega \cdot \mathrm{cm}$.[1] By way of comparison, this value is by a factor of hundred higher than that of aluminum. SRO is characterized by a high thermal and chemical stability. The compound does not disintegrate in oxidizing or inert atmospheres below $900\,^{\circ}\mathrm{C}$[2] and is almost inert against different kinds of diluted acids.[3]

Strontium ruthenate has an orthorhombic crystal structure of the $GdFeO_3$-type.[4,5] Figure 0.1(a) depicts its unit cell ($a_\mathrm{o} = 5.5730$ Å; $b_\mathrm{o} = 5.5381$ Å; $c_\mathrm{o} = 7.856$ Å[6]). The structure can be regarded as a pseudo-cubic perovskite ($a_\mathrm{p} = 3.928$ Å), as shown in Figure 0.1(b). This characteristic facilitates integration with other perovskite or perovskite-derived materials. The following example describes a situation in which the importance of the material clearly emerges.

$Pb(Zr_{0.52}Ti_{0.48})O_3$ (PZT) is a ferroelectric material with a Curie temperature of $T_\mathrm{C} = 390\,^{\circ}\mathrm{C}$.[7] This property allows the material to be used in ferroelectric capacitors for non-volatile random access memory (NVRAM) applications. The capacitors conventionally consist of a polycrystalline PZT layer sandwiched between two platinum electrodes.[8] A substantial reduction in switchable polarization after a certain amount of switching cycles (fatigue) limits the life-time of such devices. The primary reason for degradation of the ferroelectric lies in the nature of the electrode interfaces.[9] Processes like slow release of oxygen from the PZT lattice and diffusion of metal species from the electrodes are accelerated by polarization inversion. Resulting oxygen vacancy defects or platinum impurities are believed to directly cause fatigue.[10]

Fatigue is considerably reduced when conducting metal oxide electrodes – like SRO – are used. Reduction of PZT is inhibited by the presence of oxygen atoms in the electrodes and metal migration into the PZT film is impeded.[11,12] In addition, $\vec{c}$-axis oriented growth of PZT can proceed on the $(100)_\mathrm{p}$ plane of SRO (the subscript p refers to the pseudo-cubic unit cell; o will refer to the orthorhombic unit cell) with a lattice mismatch of only 2.7%. The ideal electrode-ferroelectric interface not only contributes to the reliability of these ferroelectric capacitors, but may also enhance ferroelectric characteristics like polarization.[11,13]

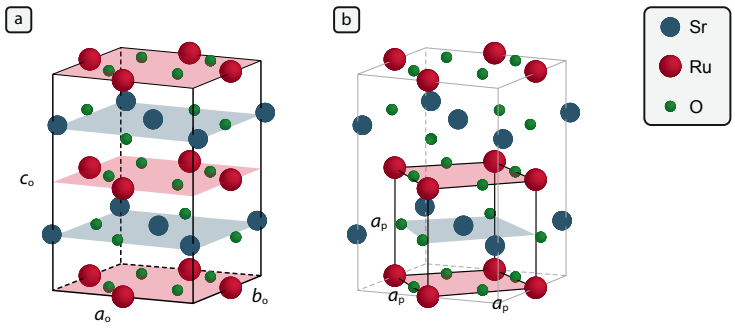

Figure 0.1: Representation of the crystal structure of $SrRuO_3$ showing the orthorhombic unit cell in (a) and the pseudo-cubic perovskite in (b).

Even though other uses of strontium ruthenate are conceivable, the material is scarcely used these days. The challenge to produce the material in a cost-effective fashion is one of the important reason why large-scale implementation is still lacking. Sputtering [11] and pulsed laser deposition [3] are conventionally used to deposit $SrRuO_3$, but both are limited by the costs of scaling up vacuum equipment and difficulties to form uniform layers over large areas.

Chemical solution deposition techniques (like sol-gel deposition) are more easily scaled and do not require high investment costs of the technology. In the past years, several ways to create thin films of $SrRuO_3$ were reported. [14–18] The methods that were proposed represent just a fraction of the possible routes that can be exploited to create thin SRO films.

In this work, attempts to grow $SrRuO_3$ thin films by polymer-assisted deposition are described. Polymer-assisted deposition is a chemical solution deposition technique, in which metal species are bound to polymers in homogeneous solutions. [19] This technique has been used mainly to form hetero-epitaxial thin films, and little is known about its applicability on arbitrary substrates. For this reason, thin films were mainly formed on oxidized silicon substrates, which are inexpensive and contain an oxide layer (at the surface) that is non-crystalline.

Homogeneous SRO precursor solutions containing polyethyleneimine complexes were prepared and studied. A standard procedure to spin cast and anneal thin films from these solutions was subseqently developed. The effect of making changes to this procedure was studied in the attempt to improve the films in terms of smoothness, density, composition, and crystallinity.

In a large part of the films that were made, protrusions were observed that had formed during the thermal treatment. These protrusions are believed to origin from energetically favorable crystallization processes, that are facilitated by large diffusion lengths of precursor species in the films during annealing. The good diffusion is caused by the films to significantly decrease in viscosity when the organics are being removed. [20] This property – that causes the success of polymer-assisted deposition in various epitaxial processes – appears to be rather disadvantageous when films are grown on substrates that can not act as templates.

Chapter 1

Theoretical background

1.1 Thin film technology

From ancient Egypt to modern science Probably no technology that is still in active development today, has a history as long as thin film technology. The antiquity of the technology is well illustrated by the remains from ancient Egyptian tombs: the majority of relics found in king Tutankhamun's tomb make an impression to be made primarily of gold, but most are covered with just thin gold layers. [21]

Furniture like a bed canopy or armchairs found in the tomb of Queen Hetepheres demonstrates how well goldsmiths had mastered thin film technology as early as 2,600 B.C. [21] The technology used to gild these objects is dissimilar from thin film technology as we know it today. First steps into modern thin film technology were made in the 1850s. Since these first steps, the technology developed into a science dominating studies in different research groups all over the world. [22]

To date, a wide variety of techniques to create thin films has been developed and applied. Three of the current techniques will be treated very briefly in the next section. For a more complete overview of thin film growth methods, the interested reader is referred to any of the excellent textbooks treating modern thin film technology. [22,23]

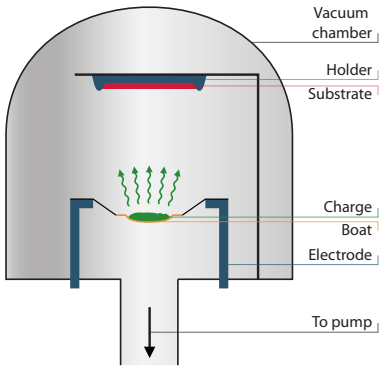

Figure 1.1: Representation of a typical evaporation system. Material (charge) is vaporized to deposit elsewhere, including on a substrate facing the charge. The figure is based on reference [23].

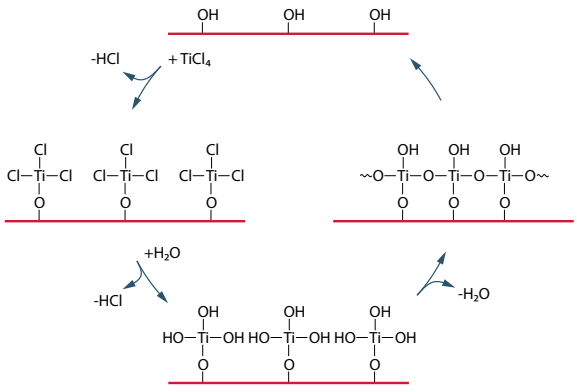

Figure 1.2: Illustration of possible reaction and processing steps to form a titania film by atomic layer depostion. The figure is based on reference [23].

Evaporation is a relatively straightforward technique and it is therefore frequently applied to deposit elemental thin films. Material is heated and evaporates from a solid source to deposit onto the surroundings, including the substrate to be coated (Figure 1.1). The method is restricted though by difficulties to form uniform films over large areas and difficulties to deposit compounds. Since the method requires vacuum, it is additionally restricted by the costs of scaling up vacuum systems. More complex system designs are usually required if mixtures are to be deposited. [23]

Atomic layer depostion (ALD) is another example of a thin film deposition method. Growth proceeds according to a self-limiting nature, *i.e.* each cycle only one atomic layer is grown atop activated surface species. Before a new atomic layer can be deposited, the surface should be re-activated by chemical means. As an example, the formation of titania layers is schematically represented in Figure 1.2. ALD allows to grow films of precisely defined thickness having excellent conformal coverage over large areas. Low deposition rates are a main drawback of the technique. [23]

Sol-gel deposition is a third and last example of a way to create thin films. The technique involves the transition of a liquid 'sol' into a solid 'gel' during the film formation process. It is one of the techniques that is counted to the group of chemical solution deposition (CSD) methods.

The general procedure to make thin films by sol-gel deposition is explained in Figure 1.3 on the basis of formation of a barium titanate ($BaTiO_3$) film. Suitable precursors are prepared, dissolved in appropriate solvents, and mixed in desired stoichiometric ratios to yield a homogeneous solution. Usually metallo-organic compounds are made (mainly carboxylates and alkoxides), because their solubility in different media can be tuned by modifying the organic parts and because these parts pyrolyse at elevated temperatures without leaving significant residues.

In the next step, a thin film is cast from the solution and allowed to dry. Gelation sets in, because the decreasing solvent content forces the precursor species to interact. In the example concerning $BaTiO_3$ film formation, condensation of Ti-precursors occurs to yield a polymeric gel. Volatile organic species are removed in a subsequent heat treatment, during which a variety of bond reorganizations and relaxation takes place. The film is crystallized in the same heat treatment step or in an additional step. Final thermal treatment is applied to produce larger perovskite grains. [25]

Lucrative aspects of sol-gel deposition include the relatively low investment costs of the technology, good control of film composition on a molecular level through control of stoichiometry of the precursor solution, and relative ease of creating thin films over large areas (especially by dip and spray coating). As for the above-mentioned film deposition methods, these strengths are counterbalanced by weaknesses. These include the inability to conformally coat three dimensional structures with a high aspect ratio and difficulties in the deposition of epitaxial, ultrathin and high density films. [20,25]

Consider the case that a uniform layer of a particular perovskite is required over an area of a few tens of square centimeters. What technique should then be used if only evaporation, ALD and sol-gel deposition are available?

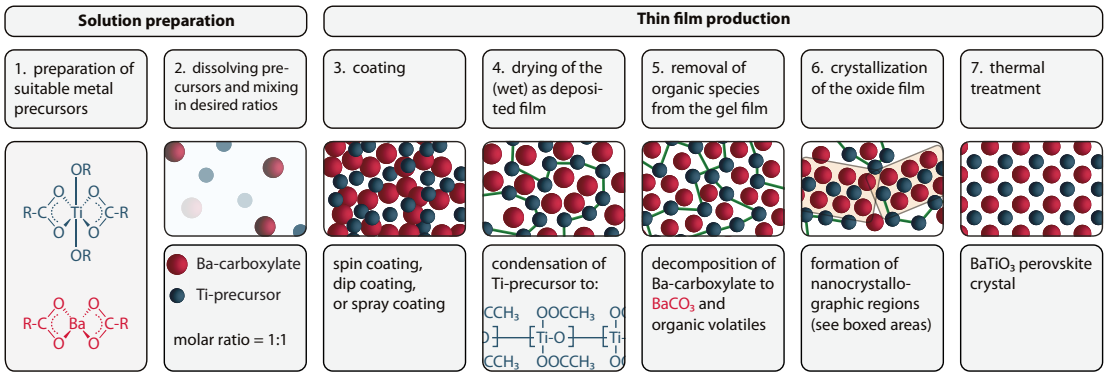

Figure 1.3: General sol-gel deposition procedure explained on the basis of formation of a barium titanate thin film (simplified). The figure is based on reference [24] and [25].

From these three techniques, evaporation can be eliminated instantly. After all, forming non-elemental films using this method is difficult. The relatively large area to be coated will be an additional barrier for using this technique. On a first glance, both ALD and sol-gel deposition seem appropriate. Which of these two methods is more suitable depends on the desired quality of the film. If a high density ultra-thin film is desired, ALD is preferred over sol-gel deposition. If on the other hand a low-cost method is sought to efficiently create perovskite films, sol-gel deposition should be selected instead.

The idea of above-mentioned examples is that no method is generally perfect for creating thin films. Selection of a method always stems from weighing the advantages and disadvantages. Since commercial thin films must pass ever more stringent demands on quality and costs, existing thin-film methods are constantly being improved and new methods are sought. Molecular beam epitaxy (MBE) is an example of a method that resulted from active development of vacuum evaporation. Polymer-assisted deposition (PAD) is an example of a technique that has received much attention lately due to recent developments made in the field.

1.2 Polymer-assisted deposition

Polymer-assisted deposition is a chemical solution deposition technique that utilizes homogeneous precursor solutions in which metal species are connected to polymers. Although the term dates back to late 2004,[19] the concept of coating thin films from homogeneous polymer-metal-complex (PMC) precursor solutions was introduced 16 years earlier.[26] Jia *et al.* boosted the interest for this CSD route by their publication in 2004.[19] A wide variety of thin films produced by PAD have been reported since then. Most research has been focussing on metal-oxide thin films,[18,19,27–33] but metal-nitride films have been studied as well.[34–37]

The key role of polymers

PAD is characterized by the various functionalities of polymers. Suitable polymers actively bind metal precursors or ions while remaining dissolved in the medium. This feature not only ensures an even distribution of metals in solution, but also impedes the metals to interact with their surroundings.[19] As a result, solutions used for polymer-assisted deposition allow to coat films of homogeneous composition and can be stable over several months.[19,20]

Besides, the viscosity of a polymeric solution can be controlled by the molecular weight and concentration of polymer in that solution. The liquid's viscosity is an important parameter for controlling film thickness in spin and dip coating processes.[38,39]

The process

The steps typically involved in polymer-assisted deposition are schematically given in Figure 1.4. This figure shows that the process – like that of sol-gel deposition – can be divided into two stages. In the first stage, a homogeneous polymeric solution containing the metal cations in their desired stoichiometric ratios is made. Thin films are subsequently prepared from this solution in the second stage.

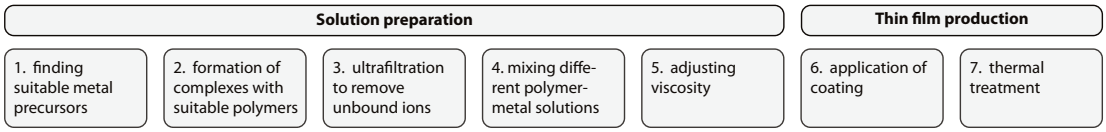

Figure 1.4: Potential steps in polymer-assisted deposition.

Polymer-assisted deposition starts by selecting suitable metal precursors, *i.e.* species that can form stable polymeric supermolecules in a desired solution. The following step is to mix these metal precursors with a polymer solution. In some cases these precursors can directly bind with a specific polymer (like in Figure 2.3(b)). In other cases complexing agents – like ethylenediaminetetraacetic acid (EDTA) – are required to bridge between the polymer and metal cations (Figure 2.3(a)).

Ultrafiltration can be applied to remove unbound ions, leaving only the desired species in solution. The concentration of metal cations within such a solution can be measured by *e.g.* inductively coupled plasma-atomic emission spectroscopy (ICP-AES). Different solutions can subsequently be mixed in desired stoichiometric ratios. If desired, the viscosity of these mixtures can be adjusted by removing solvent under reduced pressure, or by adding polymer. [19,20]

Thin films can be created from the precursor solutions by various techniques, including printing, dip coating, and spin coating. Polymer-assisted deposition is concluded by thermal treatment of the film. During this step, organic species – like polymer or complexing agents – are removed and crystallization is effected. [30]

Strengths and weaknesses of polymer-assisted deposition

Polymer-assisted deposition is a chemical solution deposition route and as such, many of its strengths and weaknesses are shared with other CSD methods. Like sol-gel deposition, low investment costs, good control of film composition and easy scaling are part of the plus-points of the technique. Unfavorable aspects like difficulties to create ultra-thin films are shared as well. [25,40] Nevertheless, polymer-assisted deposition distinguishes itself within the group of chemical solution deposition methods with its unique strengths.

A typical problem encountered with sol-gel deposition is precipitation of transition metal species out of the solution during processing, which is caused by a high reactivity of these compounds with water. [19] Titanium tetraisopropoxide for instance, reacts extensively with water and precipitates in the form of titanium hydroxydes or titanium oxides. [25] Though this problem can – for a large part – be overcome by reaction with acetylacetone (see figure 1.5), the relatively stable polymeric complexes in PAD are much less prone to precipitation. In fact, cationic species are completely shielded until the polymer is removed. [19]

Another typical difficulty encountered with sol-gel deposition is finding a solvent system that is compatible with the different organometallic precursors. Polymer-assisted deposition has been carried out with aqueous polymeric solutions for a broad range of compounds without such trouble. [19] In addition, stoichiometry control of species in solution is much more straightforward with polymer-assisted deposition than with *e.g.* sol-gel deposition. The reason is that unbound ions can be removed by ultrafiltration, whereupon the concentration of cationic species can be measured. Yet another beneficial aspect of PAD is that binding of the cations to a polymer results in a flawless homogeneous distribution of the species in solution. [20]

Typically, films up to $300\ \mathrm{nm}$ can be formed by polymer-assisted deposition without crack formation. In contrast, crack-free films grown by conventional sol-gel processes are generally limited to $200\ \mathrm{nm}$ per layer. Formation of microcracks in films formed by sol-gel deposition is explained by condensation and pore collapse of the film during heat treatment. The depolymerization process that occurs in polymer-assisted deposition does not lead to such stresses. Besides, films of higher density are generally formed with PAD compared to other chemical solution deposition methods. [20,23]

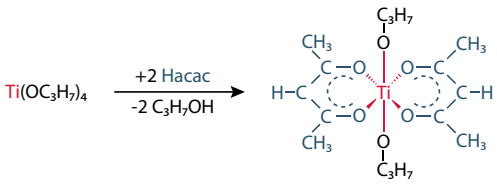

Figure 1.5: Reaction of titanium tetraisopropoxide with acetylacetone to form a significantly more stable complex due to the chelate effect and delocalization of electrons. This figure was adapted from reference [25].

Coating techniques like chemical solution deposition, chemical vapor deposition and physical vapor deposition are generally restricted in that three-dimensional objects of high aspect ratios can not be conformally coated.[25,41] Opposed to this, polymer-assisted deposition has been successfully applied to coat substrates with porous structures. Alumina membranes with well-defined straight pores of $200\ \mathrm{nm}$ in diameter were successfully coated with different metal oxide layers.[31,41] The coatings were highly uniform and did not block the channels (Figure 1.6). Evidence of conformal coating was produced by determination of the resistance of ZrO_2 coated membranes: uncoated membranes were destroyed after 15 minutes in corrosive environments, whereas coated membranes were significantly more resistant and held out for 24 hours.[41]

Another ability of polymer-assisted deposition is to control the oxidation states of metal oxides by lattice engineering, which has so far not been reported for other CSD methods. Various uranium oxides were made by choosing substrates with appropriate in-plane lattice parameters. Epitaxial UO_2 films for instance, were formed by selecting a single crystalline (100) $LaAlO_3$ substrate (Figure 1.7(a)). Conversely, hexagonal U_3O_8 films were formed from the same polymeric solution on single crystalline (001) α-Al_2O_3 (Figure 1.7(b)). Orthorhombic heteroepitaxy of U_3O_8 was found on $(1\bar{1}2)$ α-Al_2O_3. These films were found extremely stable due to the strong crystallographic pinning of the metal oxidation states.[42] With PAD, it may even be possible to make metal oxides that could not be accessed before.[20]

In the literature currently available, polymer-assisted deposition is described as a technique that not only offers the common advantages associated with CSD methods, but also removes major drawbacks conventionally linked to these methods. It allows cost-efficient bottom-up growth of crack-free, high density (epitaxial) films, which makes the technique a viable alternative to currently used thin film deposition methods.

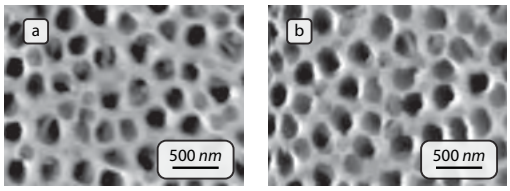

Figure 1.6: SEM images of alumina membranes with pores of $200\ \mathrm{nm}$ in diameter, being uncoated (a) and coated with ZrO_2 by PAD (b). This figure was adapted from reference [41].

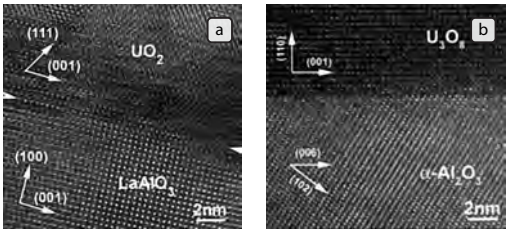

Figure 1.7: High-resolution cross-sectional transmission electron microscopy (HR-TEM) images of an epitaxial (100) UO_2 film on a (100) $LaAlO_3$ single crystal (a) and an epitaxial hexagonal (100) U_3O_8 film on a (001) α-Al_2O_3 single crystal (b). Both films were deposited by PAD from the same solution.[42]

Chapter 2

Making homogeneous metal polymeric solutions

A first aspect of polymer-assisted deposition is fabrication of stable polymeric solutions that satisfy the demands introduced in Chapter 1. Behind such solutions lies a branch of chemistry called supramolecular chemistry, which is the collective term for systems containing molecular aggregates or ions held together by non-covalent forces like electrostatic interactions or hydrogen bonding.[43]

2.1 The roots of polymer-assisted deposition

Host-guest chemistry is a distinct area of supramolecular chemistry, in which a molecular or ionic 'guest' is enveloped by a larger 'host'. Considering the case of Figure 2.1(b), the sphere will be the guest and the species surrounding it the host. Donald Cram – who shared the nobel prize in chemistry in 1987 for his work in the field – wrote: *"A host-guest relationship involves a complementary stereoelectronic arrangement of binding sites in host and guest... The host component is defined as an organic molecule or ion whose binding sites converge in the complex... The guest component is any molecule or ion whose binding sites diverge in the complex..."*.[44] Considering Figure 2.1(b) again, the four binding sites of the host converge on the central guest resulting in four non-covalent bonds depicted with dashed (red) lines.

When different guests are available, a host can prefer to interact with one of the species above others. Such selectivity may depend on factors like co-operativity of binding groups, preorganisation of the host conformation and complementarity of the host and guest binding sites.[43]

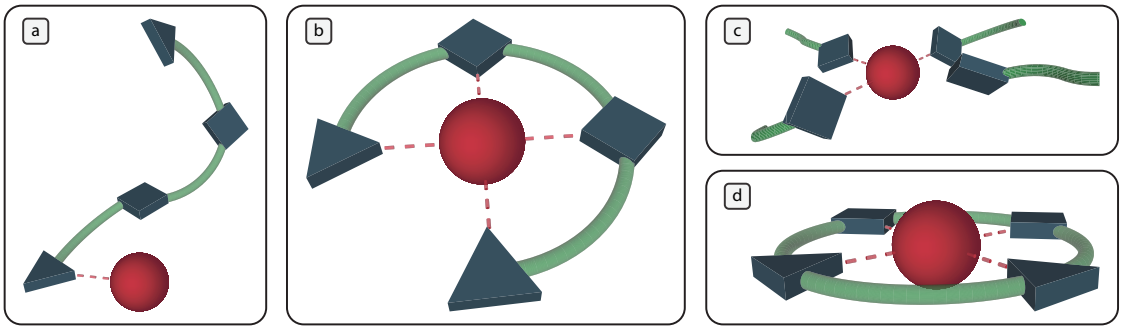

Figure 2.1: Representation of interactions in complexes. Host molecules consist of donor atoms (blue triangles and diamonds) connected to a backbone that has no active role in the complex (green tubes). Guest species are represented by red spheres and non-covalent interactions by dashed red lines.

If binding of a certain group is facilitated by the binding of another group, the groups are said to co-operate. In the case of Figure 2.1(a) one donor atom binds to a guest species, facilitating interaction between the guest and other binding sites on the same host. Every new bond that is formed adds to the stability of the complex. The complex depicted in (b) will therefore be significantly more stable than a complex that contains four individual host molecules, as represented in (c). The effect that multidentate ligands (ligands comprising multiple binding sites) form more stable complexes than unidentate complexes is called the chelate effect. It is the result of both entropic and enthalpic factors: replacing the ligands in (c) by a single ligand as in (b) yields three additional free ligands in solution, and decomplexation of complex (b) requires four bonds to be broken simultaneously.

Different from the host in Figure 2.1(b), the host in image (d) has a closed cycle and is said to be preorganized. Binding a host does not demand an energetically unfavourable change in shape of the molecule, which enhances complex stability.

Both spatially (*i.e.* of the correct size and shape) and electronically complement binding groups are beneficial for complex stability. Electronically, host-guest chemistry involves interactions between Lewis-bases and acids, which can be expressed in terms of hard and soft acids and bases (HSAB).[45,46] Hard bases have small donor atoms, having valence electrons that are not easily distorted by other charges. Conversely, soft bases have donor atoms that are larger and polarizable. Similarly, hard acids are small and non polarizable, while soft acids are large and polarizable.

Hard bases tend to coordinate with hard acids while soft bases tend to interact with soft acids. Consider the guest species in Figure 2.1 hard and the binding sites represented by diamonds softer than those represented by triangles. According to HSAB principle, coordination with triangles will likely be stronger.

Another important parameter is the inherent acid or base strength, which can also be decisive for the interactions to occur. Both softness and strength should be considered at the same time to understand coordination processes that take place. In symbols this is expressed in Equation 2.1. The values of the parameters in this equation are determined by the specific acid and base. Larger values of strength and softness lead to larger equilibrium or rate constants.[45,46]

$$logK = S_{\mathrm{A}} \cdot S_{\mathrm{B}} + \sigma_{\mathrm{A}} \cdot \sigma_{\mathrm{B}} \tag{2.1}$$

K: equilibrium constant
S: intrinsic strength
σ: softness
$\mathrm{A/B}$: acid / base

2.2 Distinguishing polymer-assited deposition

The possibilities that supramolecular chemistry offers are countless. By contrast, the field of polymer-assited deposition is curtailed considerably by the stringent demands that are made on the properties of the polymer. These properties were already introduced in the previous chapter. To date, almost solely one polymeric species has been used for polymer-assited deposition. This polymer is polyethyleneimine (PEI).

Polyethyleneimine is mainly selected because it depolymerizes at elevated temperatures, leaving almost no traces.[30,47] As shown in Figure 2.2, the polymer is converted into fractions of ethenamine during this process. Another lucrative aspect of PEI is that it contains a substantial fraction of amine groups. These groups are both able to form hydrogen bonds (Figure 2.3(a)) and interact with metal ions in solution (Figure 2.3(b)).

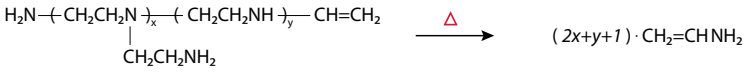

Figure 2.2: Simplified structure of PEI (on the left), which depolymerizes into ethenamine at elevated temperatures.

2.3 Preparation of a homogeneous precursor solution

The knowledge that is currently available from the fields of supramolecular chemistry and polymer-assited deposition gives a starting point for the search for stable polymeric solutions containing strontium and ruthenium species. The synthesis of one such solution is described in this section.

All chemicals used were bought from commercial suppliers and were used without further purification. Additional information about the used chemicals is given in Table 2.1. Ultrapure water with a resistivity of $18.2\ \mathrm{M\Omega \cdot cm}$ was obtained from a Smart 2 Pure water purification system (TKA).

Acidity was monitored by an AR15 pH meter (Accumet research). Density was measured by pipetting $5\ \mathrm{ml}$ solution in a $5\ \mathrm{ml}$ vial and measuring weight on an analytical balance. The average density calculated over three measurements was used. Viscosity was measured in an automated micro viscometer (Anton Paar) at $25\,^{\circ}\mathrm{C}$ and averaged over ten measurements.

Synthesis of strontium precursor solution

In a $5\ \mathrm{ml}$ glass screw cap vial containing a stirring magnet, $500\ \mathrm{mg}$ branched polyethyleneimine with an average molecular weight of $10,000\ \mathrm{g \cdot mol^{-1}}$ were added to $2.5\ \mathrm{ml}$ water. The mixture was vigorously stirred (at $\sim 1000\ \mathrm{rpm}$) until the polymer had completely dissolved. A total of $449\ \mathrm{mg}$ ($1.52\ \mathrm{mmol}$) ethylenediaminetetraacetic acid (EDTA) was subsequently added. Vigorous stirring was continued for approximately twenty minutes until the solution had turned clear and colorless again.

A $0.6\ \mathrm{M}$ aqueous solution of $Sr(NO_3)_2$ ($321\ \mathrm{mg}$; $1.50\ \mathrm{mmol}$) was prepared. This solution was added dropwise within approximately five minutes to the first solution, which was vigorously stirred. The resulting colorless solution was stirred moderately ($\sim 500\ \mathrm{rpm}$) for at least one hour. A similar procedure was proposed by Jain *et al.*[30]

Synthesis of ruthenium precursor solution

A solution containing $500\ \mathrm{mg}$ PEI ($10,000\ \mathrm{g \cdot mol^{-1}}$) in $2.5\ \mathrm{ml}$ water was prepared. While vigorously stirring this solution, pH was adjusted to $6 - 6.5$ by adding an aqueous solution of $37\,\%\ w/w$ hydrochloric acid ($19 - 24$ drops).

A total of $392\ \mathrm{mg}$ ($1.50\ \mathrm{mmol}$) $RuCl_3 \cdot 3\,H_2O$ was dissolved in $2.5\ \mathrm{ml}$ water and vigorously stirred for at least one hour. The very dark chestnut brown solution was then added dropwise within approximately fifteen minutes to the polymeric solution, which was vigorously stirred. The resulting solution was moderately stirred for at least one hour.

Chemical	**CAS**	**Supplier**	**Purity**	**M.W.** $\mathbf{(g \cdot mol^{-1})}$
4,4'-dimethyl-2,2'-bipyridine	1134-35-6	Fluka	$\geq 99\,\%$	184.24
ethylenediaminetetraacetic acid	60-00-4	Acros Organics	$\geq 99\,\%$	292.23
polyethyleneimine, branched	9002-98-6	Alfa Aesar	$\geq 99\,\%$	600 1,800 10,000
			30 % w/w aq. soln.	50,000–100,000
potassium dichromate	7778-50-9	Fluka	$\geq 99.0\,\%$	294.18
ruthenium(III) chloride trihydrate	13815-94-6	Aldrich	$\geq 99.9\,\%$	261.47
strontium nitrate	10042-76-9	Fluka	$\geq 99\,\%$	211.63

Table 2.1: List of chemicals used during the synthesis of the precursor solutions.

Combination

The strontium precursor solution was transfered to a $25\ \mathrm{ml}$ glass screw cap bottle containing a stirring magnet. While vigorously stirring this solution, the complete ruthenium solution was added within one minute. Moderate stirring was pursued for at least one complete day after which the solution was stored. Properties of this solution are given in Table 2.2. Just before spin coating the solution, it was stirred for at least five minutes.

pH	4.5
density	$1.10\ \mathrm{g \cdot mol^{-1}}$
dynamic viscosity	$3.0\ \mathrm{mPa \cdot s}$

Table 2.2: Properties of the standard precursor solution.

2.4 Chemistry behind the precursor solution

Supramolecular complexes that resulted from the synthesis routes described in the previous section may be represented by the structures depicted in Figure 2.3(a) and (b). The most marked difference between the two is that Ru(III) cations are connected directly to the PEI backbone, while Sr(II) cations are connected indirectly via an EDTA complex. The reason for this distinction is related to the different properties of Sr(II) and Ru(III) cations.

The electron configuration of Sr(II) is similar to that of krypton: it contains well protected valence electrons in completely filled sub-shells. Ru(III) has a [Kr]$4d^5$ configuration, in which the d electrons are more easily distorted by charges. The absence of $5s$ electrons further increases polarizability of the $4d$ electrons. For these reasons, Ru(III) cations fall in the group of borderline acids whereas Sr(II) cations are classified as hard.[45]

Besides softness, the two cationic acids differ in strength. Since they have a smaller ionic radius and a higher positive charge, Ru(III) cations are considerably stronger acids than Sr(II) cations. The intrinsic strength parameters will therefore have an important influence on the equilibrium and rate of complex formation when Ru(III) cations are involved (Equation 2.1). Conversely, softness will have a more substantial effect during the course of complexation of Sr(II) cations.

To understand why interactions are as proposed in Figure 2.3, the bases should be classified as well. The softness of bases generally decreases in the sequence Cl $\sim$ N $>$ O.[48] The same sequence is found for increasing electronegativity, which is obviously linked to polarizability. Not only the donor atom, but also the groups attached to it determine the softness of bases. The different amine groups on PEI will therefore not be of equal softness.

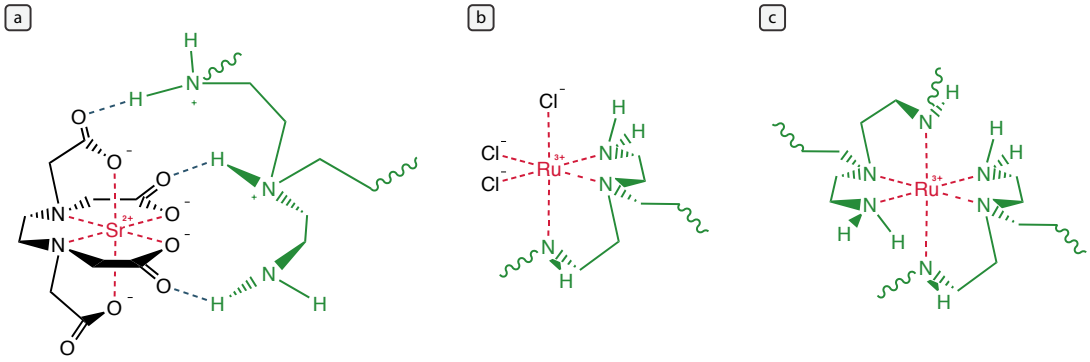

Figure 2.3: Image (a) shows part of a supermolecule that contains complexes of Sr(II) cations and EDTA hosts which are linked to a PEI backbone. Supramolecular complexes of Ru(III) and PEI are found in image (b) and (c).

The strength of donor groups will be influenced by their local structure. Carboxylate anions on EDTA are stabilized by resonance with neighboring oxygen atoms, which decreases the strength of these bases. Concerning the amine groups, base strength will increase in the order tertiary $>$ secondary $>$ primary, because induction of electrons from attached hydrogen atoms is higher than from carboxyl groups.

Hard and weakly acidic Sr(II) cations will tend to interact with the oxygen coordinating groups on EDTA, which are harder than other electron donors in solution. Co-operativity of the six donor atoms in EDTA will considerably contribute to the stability of a complex formed with this ligand. The supramolecular complex that is depicted in Figure 2.3(a) is therefore the logical result of the different interactions in solution.

Borderline and strongly acidic Ru(III) will preferably interact with amines instead of carboxylates. Direct interactions with the polymer backbone become preferred over a six-fold EDTA embrace. Co-operative interactions with three amine groups on PEI will add up to the stabilities of the structures shown in Figure 2.3(b) and (c).

The formation of complexes involving different PEI molecules (Figure 2.3(c)) unconditionally results in loss of solution homogeneity by cross-linking of a multiple of polymers. This is thought to occur when the polymeric solution is not acidified before adding the aqueous solution containing Ru(III) cations. After adding the first drop, dark brown, millimeter-sized flakes were found dispersed in a light brown solution.

Acidification of the polymeric solution with hydrochloric acid leads to protonation of the amine groups on PEI, which consequently weakens interactions with Ru(III) species. Furthermore, the increased amount of chlorine ions in solution results in a higher probability of interaction between these species and Ru(III) cations. Formation of the complex in Figure 2.3(b) will now become more likely, while formation of the complex in (c) will be suppressed.

2.5 Analysis of the precursor solution

Thermogravimetric analysis and differential scanning calorimetry Thermogravimetric analysis (TGA) and differential scanning calorimetry (DSC) were simultaneously conducted on the precursor solution. An aliquot of the solution was placed in a metallic sample crucible which was placed in a Jupiter STA 449 F3 thermo-microbalance (Netzsch). The solution was allowed to dry at room temperature, while the system was flushed with a mixture of nitrogen and oxygen, or pure nitrogen gas. After the sample weight had stabilized, measurements were started. The temperature was increased with $5\,^{\circ}\mathrm{C} \cdot \mathrm{min}^{-1}$ and the gas flow was maintained constant at $70\ \mathrm{cm}^3 \cdot \mathrm{min}^{-1}$.

Two experiments that varied from each other in gas flow composition were conducted. A first experiment was performed in a mixture of nitrogen and oxygen (in a N_2:O_2 volume ratio of 6:1). This experiment forms the basis of the discussion in the next paragraphs. The results are plotted with opaque curves in Figure 2.4. A second experiment was performed in a pure nitrogen gas stream. Results from this experiment are given in the same figure by transparent curves.

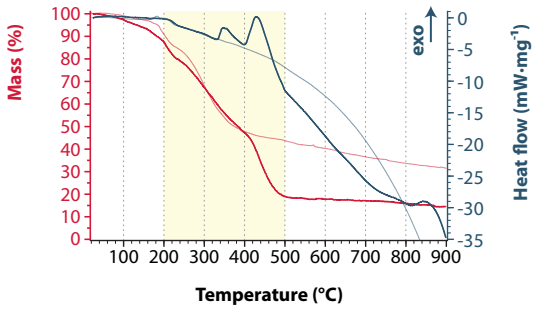

Figure 2.4: Combined TGA and DSC data for the standard precursor solution. The opaque curves were obtained in an environment containing nitrogen and oxygen (volume ratio 6:1); the transparent curves were obtained in a pure nitrogen gas stream.

The results are divided into three main regions. Residual water, together with chlorides and nitrates in solution, was removed below $200\,^{\circ}\mathrm{C}$. A total weight loss of 12% went together with no significant thermodynamic events in this first region. Decomposition of organic fractions and disintegration of complexes set in at $200\,^{\circ}\mathrm{C}$ and proceeded up to $500\,^{\circ}\mathrm{C}$. A significant decrease in weight of 69% was measured, together with two exothermic events. Above $500\,^{\circ}\mathrm{C}$ weight loss was limited indicating that no major decomposition took place. An exothermic event at $845\,^{\circ}\mathrm{C}$ stands out against the endothermic course of the DSC signal in this region. Endothermic processes that may have taken place are *e.g.* decomposition of residual organics and volatilization of metal species.

Main decomposition events took place in the second (highlighted) region, which can be divided into different stages. About 8.5% of the original mass was lost in a first stage between 200 and $235\,^{\circ}\mathrm{C}$. This loss was attended with a small exothermic peak in the DSC signal. Possibly monodentate guests on ruthenium hosts (Figure 2.3(a)) were removed at this stage. Decomposition of organics commenced directly hereafter and proceeded up to $500\,^{\circ}\mathrm{C}$. PEI probably started to decompose before EDTA, because EDTA was stabilized by interactions with strontium cations.[49]

The exothermic curve ($4.1\ \mathrm{kJ}\cdot\mathrm{g}^{-1}$) with an onset temperature of $404\,^{\circ}\mathrm{C}$ and a peak at $429\,^{\circ}\mathrm{C}$ coincides well with the measured sharp decrease of mass between 400 and $500\,^{\circ}\mathrm{C}$. Both the exothermic curve and steep mass decline are absent in the data from the experiment performed in N_2. There is thus every indication that combustion of organic residues took place in this region. This is at odds with allegations made before about the decomposition behavior of PEI and EDTA. Burrell and co-workers for instance claim that non combustion processes of PEI and EDTA take place that *"result in extremely clean metal oxide films even in inert or hydrogen atmospheres"*.[20]

The two other exothermic peaks at $346\,^{\circ}\mathrm{C}$ ($0.8\ \mathrm{kJ}\cdot\mathrm{g}^{-1}$) and $845\,^{\circ}\mathrm{C}$ ($2.0\ \mathrm{kJ}\cdot\mathrm{g}^{-1}$) do not coincide with the TGA signal and are most probably due to crystallization of RuO_2 and $SrRuO_3$, respectively. Preliminary formation of RuO_2 was already observed in thin films that were spin cast on different substrates from different solutions.[14,16,17] Additional evidence for the formation of RuO_2 before the formation of $SrRuO_3$ is provided in Chapter 4.

Stability of the precursor solution

The stability of the precursor solution was checked in a period exceeding two and a half months. During this period, thin films were made from one and the same solution at different ages (the procedure to make thin films is described in Chapter 3 on page 20). Topographical characterization of these films was performed by atomic force microscopy. The films produced had similar appearances and a root mean square roughness of $7.0 \pm 1.5\ \mathrm{nm}$. These results indicate that the solution had been stable for several months.

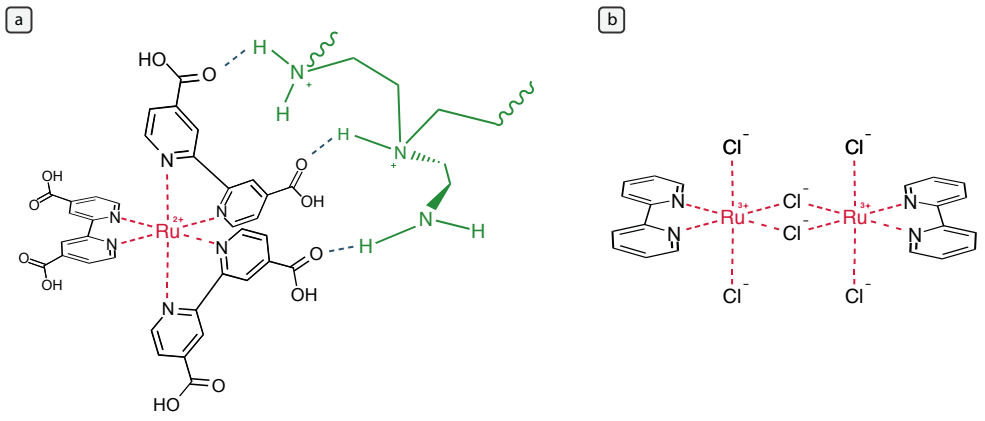

Figure 2.5: Representation of tris-(4,4'-dicarboxy-2,2'-bipyridine)-ruthenium(II) interacting with PEI (a) and trichloro-(2,2'-bipyridine)-ruthenium(III).

Some thin films were made after filtering the solution through a Spartan 30/0.2 RC filter unit (Whatman; particle retention $0.2\ \mu\mathrm{m}$) just before spin coating. This extra step in the manufacturing process had no effect on the final topography of the thin film. Because equal films were produced, it is plausible to consider the solution homogeneous.

2.6 Alternative precursor solutions

The solution described and studied in the previous sections was not the only solution that was prepared. Three different solutions are worth mentioning, which will be referred to as solutions $\mathbf{2}$, $\mathbf{3}$, and $\mathbf{4}$. Solution $\mathbf{1}$ denotes the solution described above.

None of the alternative solutions was extensively studied or used. Regarding solutions $\mathbf{3}$ and $\mathbf{4}$, the reason can be found in the poor solubility of the complexes in aqueous polymeric solutions. Complete descriptions of the corresponding syntheses are outside the scope of this chapter, but are described in Appendix A instead. This section serves to give a brief description of the intended solutions.

Solution $\mathbf{1}$ forms a mixture of two kinds of polymeric supermolecules. The first kind ideally contains only strontium precursor species, and the second kind solely consists of ruthenium precursors. In other words, the solution can be regarded as a mixture of two different kinds of 'spaghetti'. Attempts were made to form a single supramolecular species in which the strontium and ruthenium precursors were intermixed between the polymeric chains. The reason to do so, was that the precursor species are even more homogeneously distributed in such solutions. Two approaches were developed to form this kind of SRO precursor solution (see Appendix A). The two solutions were called $\mathbf{2a}$ and $\mathbf{2b}$.

The idea behind solution $\mathbf{3}$ was to make a ruthenium complex that could be linked to the polymer backbone via hydrogen bonding. The intended complex – linked to PEI – is represented in Figure 2.5(a). This complex will have a different thermal stability compared to that used in the original solution. It will thus be released at a different moment during the thermal treatment of spin cast films, which will influence the film forming processes. Ideally, strontium and ruthenium are released simultaneously during the annealing process, and crystallization takes place at the same time.

The intended approach for solution $\mathbf{4}$ was to block two of the six co-ordinating sites of the Ru(III) cations by one equivalent of 2,2'-bipyridine (Figure 2.5(b)). With two of its co-ordinating sites blocked, ruthenium will not tend to cross-link two polymer chains. This cross-linking process was believed to take place in the original solution when no pH adjustments were made, leading to a loss of homogeneity of the solution (further details can be found on page 15). Although the solubility of the ruthenium complex in solution $\mathbf{4}$ was very low, adding small amounts of the (solid) complex to an aqueous PEI solution did not give flakes or other kinds of precipitation. This indicates that, by blocking co-ordinating sites on the ruthenium hosts, cross-linking will indeed be inhibited.

Chapter 3

Creating and analyzing thin films: the standard procedure

3.1 The concepts of spin coating and processing thin films

Spin coating With the precursor solutions defined in the previous chapter, thin film can be produced. Preparation of thin films was realized by spin coating. During spin coating, a small amount of liquid is dispersed evenly over a rotating substrate. Spin coating typically consists of four stages. In a first stage, solution is delivered onto the center of a substrate. During a subsequent spin-up stage, centrifugal forces disperse the liquid over the substrate. Excess liquid leaves the substrate during the spin-off stage. Evaporation overlaps every stage, but takes over from the spin-off stage when flow is no longer possible. [23]

In typical spin coating processes, three variables are controlled: spinning time, angular acceleration, and angular velocity. Thickness of final ceramic films will be determined by many different variables, including these three. Examples of other variables of influence are the humidity and temperature of surrounding air, the nature of the solvent, and the concentration and nature of solutes. The film thickness is largely a balance between shearing of the liquid and drying rate. It is generally proportional to the liquid viscosity – which is linked to the drying rate – but inversely proportional to the spinning speed and time. [50]

Thermal treatment

Thermal treatment of spin-cast thin films is applied to both remove the organic constituents and induce crystallization. Two approaches can generally be used: the one-step and two-step process. In the two-step process, most of the organic moieties are removed in a separate processing step prior to crystallization. Films are heated directly to the crystallization temperature in the one-step process. [25] Both the one-step*e.g.* [19,33] and two-step*e.g.* [27,32] processes are reported for the production of thin films by polymer-assisted deposition.

Organic fractions are removed either by thermolysis (non-combustion processes) or pyrolysis (combustion processes). Which of, and to what extent these processes occur depends on factors like the precursor chemistry employed, heating rate, temperature, and atmosphere. In any case, the polymeric thin films made by PAD are *"effectively molten"* during thermal decomposition (*i.e.* their viscosities decrease substantially). [20] This provides effective mixing of precursor species even at this stage.

Crystallization advances via nucleation and growth processes. Nucleation can commence either at the substrate interface, at the surface of the film, or in the bulk. The driving force for crystallization is an important parameter that influences the energy barriers of these nucleation events as well as the nucleation rate. The thermal energy available during crystallization determines which barriers can be overcome and by this, the microstructure. [25,38]

Another important parameter determining the thin film morphology is the precursor chemistry. For PAD processes in particular, true bottom-up growth is facilitated if the removal of the polymer and crystallization occur concurrently.[20] The reason lies in the large diffusion lengths of metal species due to the low viscosity of the thin film during the decomposition of the polymer.

Only in this brief introduction on spin coating and processing thin films, plentiful parameters were identified that control the shape, composition or crystallinity of final films. Every stage in a thin film production process – from solution chemistry to the final thermal treatment – needs to be carefully optimized in order to create desired ceramic films. The process of making $SrRuO_3$ thin films by polymer-assisted deposition forms no exception. Before the effects of tuning variables can be studied, a standard procedure should be defined first. The standard procedure and resulting films are treated in this chapter.

3.2 A standard procedure for making thin films

Oxidation of silicon substrates Boron doped p-type CZ-silicon (001) wafers (Okmetic) were oxidized under ambient atmospheric conditions without any preceding cleaning procedure. Oxidation was carried out in a laboratory chamber furnace (Carbolite) heated from room temperature to $1100\ ^{\circ}\mathrm{C}$ at $4\ ^{\circ}\mathrm{C}\cdot\mathrm{min}^{-1}$. Once the furnace had reached $1100\ ^{\circ}\mathrm{C}$, it was kept at this temperature for five hours after which it was allowed to cool down to room temperature. The penetration depth of the oxide into the silicon wafers was estimated by cross-sectional high-resolution scanning electron microscopy to be $200\ \mathrm{nm}$.

Substrate cutting and cleaning

Square substrates of approximately $1.5 \times 1.5\ \mathrm{cm}^2$ were made from the wafers. Just before spin coating a thin film, a substrate was cleaned in two steps. In the first step, organic residues and (dust) particles were removed from the substrate by exposing it to a jet of super critical CO_2 ice crystals. During this process, the substrate was kept on a heated surface at approximately $250\ ^{\circ}\mathrm{C}$ by application of a vacuum to the backside. This step took about two minutes per substrate.

In the second step, the substrate was transferred to an oxygen plasma cleaner (Harrick). The plasma chamber was rinsed two times by first reducing the pressure inside the chamber to a value below $10\ \mathrm{mbar}$, and then venting the chamber with O_2 until a pressure of approximately $900\ \mathrm{mbar}$ was reached. The chamber was then brought to a vacuum below $1\ \mathrm{mbar}$, after which a plasma of low energy was created. The plasma – which could be observed by a faint purple glow – was maintained for two minutes.

Spin coating

A micro fragment adapter ($> 3\ \mathrm{mm}$) was placed on top of the vacuum center chuck in a WS-400-6NPP-LITE single wafer spin coater (Laurell Technologies). The substrate was released from the plasma chamber and placed on top of the adapter. The substrate was held in place by applying a vacuum to the backside of the substrate through the micro fragment adapter and center chuck.

An amount of $600\ \mu\mathrm{l}$ of solution **1** was placed on the middle of the substrate. Immediately hereafter, the spinner was accelerated with $550\ \mathrm{rpm}\cdot\mathrm{s}^{-1}$ to $2500\ \mathrm{rpm}$. After spinning for two minutes, the spinner was decelerated with $550\ \mathrm{rpm}\cdot\mathrm{s}^{-1}$ until it came to a halt. The substrate was quickly placed on a hot stage at $180\,^{\circ}\mathrm{C}$, where it was kept for about ten minutes.

Thermal treatment

The substrate with the (physical gel) film was placed in the laboratory chamber furnace at room temperature. The furnace was heated with $4\,^{\circ}\mathrm{C}\cdot\mathrm{min}^{-1}$ to $850\,^{\circ}\mathrm{C}$ at which it was kept for three hours. The furnace was subsequently allowed to cool to room temperature.

3.3 Ways to analyze thin films

Thin films produced with the standard procedure were analyzed by three techniques: optical microscopy, atomic force microscopy (AFM), and X-ray diffraction (XRD). Additional techniques were used to gain insights in the development and nature of thin films made by deviating from the standard procedure. Although these results are not included in this chapter, descriptions of all analysis methods used for obtaining the results discussed in this report are given in this section.

Topographical analysis

Topographical analysis of thin films was performed by a set of three techniques. First and foremost, films were investigated with an Eclipse ME600 optical microscope (Nikon). Particularly dark field images with a magnification of $50\times$ gave a good first impression of the roughness of the films.

Most samples were analyzed in a Dimension Icon atomic force microscope (Veeco). Measurements were conducted somewhere in the centre of the substrate over an area of mostly $5\times5\ \mu\mathrm{m}^2$. Particularly tapping mode AFM was used, but contact mode was used as well.

AFM height images give a clear idea of the morphology of thin films. Besides the qualitative information height images offer, various quantitative information can be obtained as well. The root mean square (RMS) roughness of films was calculated from AFM height images by an algorithm that was built in the analysis software (Gwyddion 2.19). The equation used for calculating RMS roughness values is given in Equation 3.1.

$$R_{\mathrm{RMS}} = \sqrt{\frac{\sum_{i=0}^{n} z_{\mathrm{i}}^2}{n}} \tag{3.1}$$

R_{RMS}: root mean square roughness
n: the total amount of height data points in a single image (512×512)
z_{i}: the measured height at data point i, relative to the lowest datapoint in the series

Selected samples were further studied in a CTR6000 high-resolution scanning electron microscope (Leica). Samples were examined by both top views and cross sectional views. Cross sectional high-resolution scanning electron microscopy (HR-SEM) images contain additional information about the thickness of the films.

Crystallographic and compositional analysis

The crystallographic structure in thin films was studied on a PW 1180 X-ray powder diffractometer (Philips). The $\omega - 2\theta$ (gonio) or 2θ (glancing incidence) measurements were most frequently performed. In both of these cases, the 2θ axis was scanned between 10^{o} and 80^{o}.

Although scan settings were changed frequently, most $\omega - 2\theta$ scans were performed with a step size of 0.05^{o} (in 2θ), measuring five seconds per step. Most 2θ measurements were performed at $\omega = 1.5^{\mathrm{o}}$ under continuous spinning of the sample (with a revolution time of 1 second). X-rays were counted for ten seconds per step of 0.05^{o}. The backgrounds of most spectra were subtracted by an algorithm built in the analysis software (X'Pert HighScore Plus 2.1).

Elemental studies on selected thin films were conducted by both energy dispersive X-ray spectroscopy (EDX) and X-ray photoelectron spectroscopy (XPS). EDX was performed in the high-resolution scanning electron microscope with an electron acceleration voltage of $10\ \mathrm{keV}$ applied. Acquisition times of $100\ \mathrm{s}$ (live-time) were used.

XPS was performed in a Quantera SXM scanning XPS microprobe (Physical Electronics) with monochromatic Al K_α radiation. Areas were scanned with a beam size of $100\ \mu\mathrm{m}$ and specific points with a beam size of $9\ \mu\mathrm{m}$. The detector was aligned at 45^{o}, relative to the substrate surface.

3.4 A thin film from the standard procedure

Dark field optical microscopy and tapping mode AFM images of a thin film that resulted from the standard procedure are included in Figure 3.1. These images show that the film is characterized by a continuous layer from which circular areas – of about $1\ \mu\mathrm{m}$ in diameter – protrude. These protrusions are on average not higher than $20\ \mathrm{nm}$, but contain smaller projecting particles that can exceed $80\ \mathrm{nm}$.

The development of protrusions

Regardless of their composition, the formation of protrusions is undesired in the process to make thin films of $SrRuO_3$. After all, the film roughness is drastically determined by the presence of this kind of microstructure. Finding the cause of the development of protrusions may yield ideas for adaptations to the standard procedure that may inhibit their formation.

To investigate at what stage protrusions were formed, films were studied during different steps in the production process. Figure 3.3 shows images of a film after it was spin cast and kept on a hot stage. The absence of microstructure on this film indicates that protrusions are formed during the final step of the film forming process.

A possible explanation for the formation of protrusions is given in Figure 3.2. Metal species that are released from the complexes can easily diffuse due to the low viscosity of the decomposing thin film. Different particles that are released will interact with each other and will tend to combine in order to reduce the total surface energy. Condition for this process to occur is that the metal cations are either reduced to their elemental form or that combination of metal cations is accompanied by incorporation of a counter ion (like O^{2-}). Any simultaneous occurring crystallization events may greatly add to the driving force behind the formation of the protrusions.

If this scenario is correct, the formation of the protrusions can be impeded in several ways. Adjusting the solution composition to give more stable metal complexes for example, may lead to delayed metal release after the decomposition of the polymer has completed. This way the viscosity of the film will be significantly higher when crystallization takes place, compared to the case that crystallization and depolymerization occur simultaneously. Another way is to control the depolymerization process of the polymer by *e.g.* changing the heating rate, which will also effect the diffusion lengths inside the thin film.

3.5 Reproducibility

In order to check the reproducibility of the standard method, new films were made. Figure 3.4 shows a film made two months after that of Figure 3.1. In both cases, the standard procedure was followed as good as possible and even the ages of the solutions were comparable. Nevertheless, clear differences can be discovered between the two samples.

In the case of Figure 3.4, protrusions are significantly smaller and form a maze over the substrate. Particles of high aspect ratios are still present, but are more uniformly dispersed over the area. Several causes may have resulted in the poor reproducibility, like variations in the solution content or atmospheric humidity. This matter will be pursued in greater depth in the following chapter.

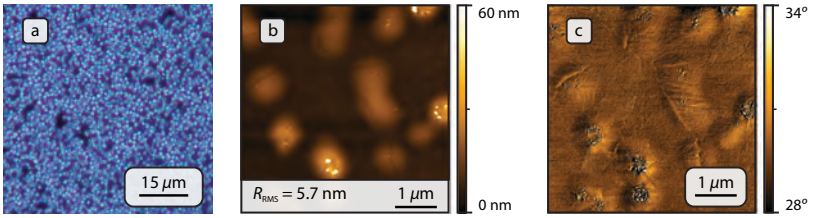

Figure 3.1: Dark field $50\times$ optical microscopy image (a), and tapping mode AFM height (b) and phase (c) images of a thin film made by the standard procedure with a three days old solution.

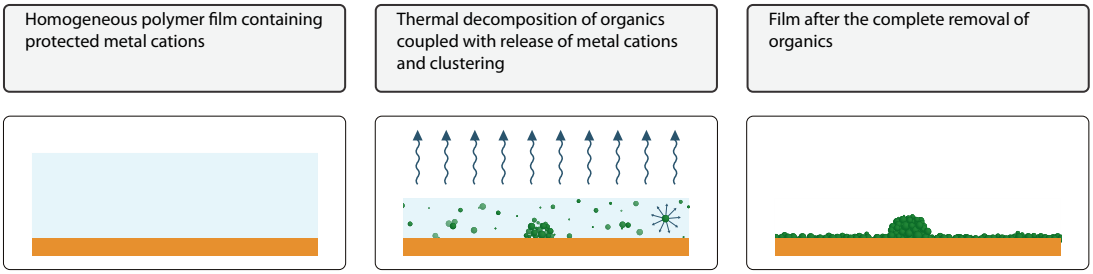

Figure 3.2: Simplified representation of a scenario for formation of protrusions, in which clustering of metal species is driven by a reduction in surface energy. Diffusion of species is facilitated by the low viscosity of the decomposing thin film.

The development of surface undulations

The maze of protrusions in the thin film of Figure 3.4, bear much resemblance to two-dimensional simulations of decomposition at the spinodal of single phase fluid systems.[51] Similar thickness variations on thermodynamically stable polymeric thin films were found previously.[52,53] Because the similarity is so striking, a second scenario for the formation of protrusions is taken into account. In this scenario, 'spinodal-like dewetting' is expected to cause the surface roughening observed in Figure 3.4(b).

The processes behind the formation of the surface undulations on stable polymeric thin films is well understood. For these thin films, the beginnings of corrugation processes are related to thermal fluctuations.[52] A similar explanation will possibly not apply in the present case. Most thermal fluctuations are expected when the substrate is placed on the hot stage just after a thin film has been cast atop. During the following thermal treatment, these fluctuations are thought to be minimized by the comparatively small heating rate of only $4\ ^{\circ}\mathrm{C} \cdot \mathrm{min}^{-1}$. If the corrugations would have developed due to thermal fluctuations, this process would have most probably happened already on the hot stage. However, Figure 3.3 already revealed that corrugations did not develop during this stage. The more likely scenario is that the surface undulations originate from local composition variations in the thin film that developed during decomposition of the organics. Decomposition of organics will lead to density variations and eventually to film roughening.

Subsequent growth of surface waves has been explained by action of long range Van der Waals forces. These forces can lead to amplification of the surface waves if they exceed the negative energy that is created when species diffuse to the thicker parts of the film.[52] Van der Waals actions may also have caused the growth of surface undulations in the present case, but again the process is thought to be deviant.

When a surface is corrugated, a pressure gradient develops in the film described by the Young-Laplace equation (3.2). The local increase in pressure at the convex regions can be reduced by restoration of the flat surface or by delivery of species of lower surface energy from the bulk of the film. If the latter process is dominating, corrugations will spontaneously grow.

If corrugations are indeed formed by a spinodal-like dewetting process, different measures are conceivable to inhibit their formation. By slowing down the decomposition of organics, the mobility inside the thin film is reduced and the formation of surface undulations is hindered. Besides, the

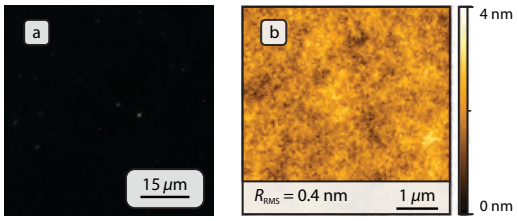

Figure 3.3: Dark field optical microscopy image (a) and tapping mode AFM height image (b) of a film after solvent removal on a hot stage.

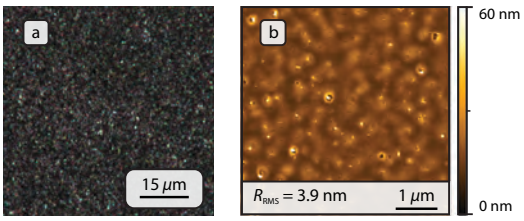

Figure 3.4: Dark field optical microscopy image (a) and tapping mode AFM height image (b) of a thin film made by the standard procedure with a solution being three days old. This thin film was produced two months after that of Figure 3.1.

atmosphere during the decomposition of organics will influence the tensions in the surface and will contribute to the formation of surface undulations. Also the film thickness may influence the coarse of fluid flow inside the thin film. The effects of changing parameters in the production process are discussed in the next two chapters.

$$P^{\alpha} - P^{\beta} = \frac{2\gamma}{r_{\mathrm{m}}} \tag{3.2}$$

P:	pressure
γ:	surface tension
r_m:	radius of curvature that is positive when it lies within phase α
α/β:	phase α/β

Chapter 4

Understanding processes taking place during thermal treatment

The analysis of the thin films described in previous chapter gave insights into their development. These results also raised several questions, particularly on the changes that are induced at the thermal treatment stage. Understanding of the processes that occur at this stage is a step forward in the search for a method to produce smooth $SrRuO_3$ thin films.

This chapter will focus on the processes that occur during thermal treatment. To gain extra insights, thin films were produced by deviating from the standard procedure. In many of the cases, deviations were made on various parameters. Full descriptions of all changes made with respect to the standard procedure are not included in the text parts, but can be found in the captions of corresponding figures instead.

4.1 The shape of protrusions and their relation with the annealing temperature

Protrusions develop during the thermal treatment stage. More precisely, they are expected to develop during the depolymerization process. The TGA results in Figure 2.4 imply that this process will have completed before $500\,^{\circ}\mathrm{C}$ is reached. In the standard procedure, thin films are exposed to a maximum temperature of $850\,^{\circ}\mathrm{C}$. If the assumption is correct, protrusions have already developed at a lower temperature. To verify this, thin films were annealed at $600\,^{\circ}\mathrm{C}$ as well.

A resulting thin film is compared to thin films annealed at $850\,^{\circ}\mathrm{C}$ in Figure 4.1. Films annealed at $600\,^{\circ}\mathrm{C}$ contain protruding features with both round and sharp edges. These protrusions are considerably higher than those observed on thin films annealed at $850\,^{\circ}\mathrm{C}$. The sharp edges in these features indicate that the material may be crystalline. On the films annealed at $850\,^{\circ}\mathrm{C}$, raised circular areas exist. These areas have a considerably higher roughness than the surrounding film. From this point, different designations will be used to discriminate between the two kinds of protrusions. The features observed in image (a-c) will be called hills and the features observed in image (d-f) craters.

The absence of hills on the films annealed at $850\,^{\circ}\mathrm{C}$ does not mean that no hills were formed during annealing. The opposite may be true and explains the shape of the craters observed in these images. A conceivable scenario is that hills were formed but decomposed between $600\,^{\circ}\mathrm{C}$ and $850\,^{\circ}\mathrm{C}$. The residue of the hills formed the craters.

In the previous chapter, two scenarios were introduced to explain the development of protrusions in thin films. In a first scenario, protrusions are supposed to develop in the film due to diffusion of particles that tend to combine in order to reduce the total surface energy. In a second scenario, protrusions are expected to form by convection processes that are initiated by instabilities in the film, resulting in undulations on the surface.

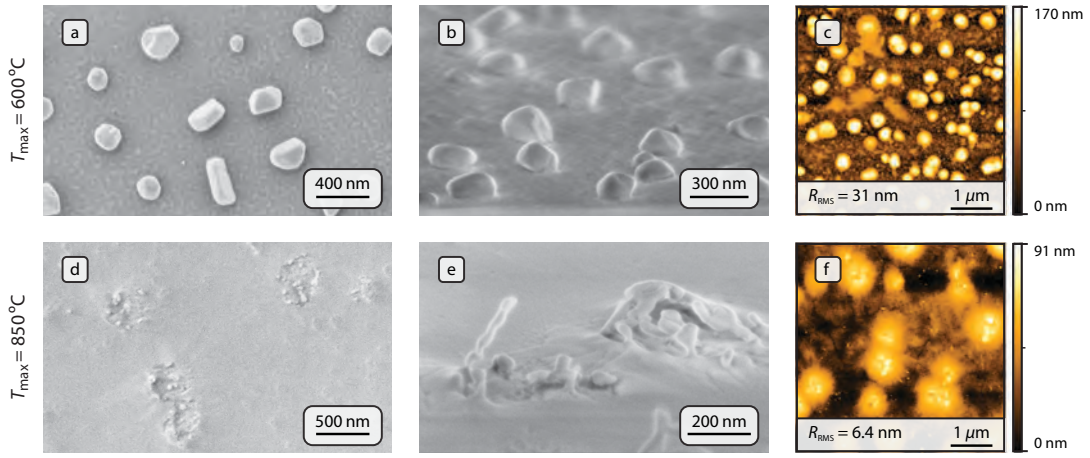

Figure 4.1: HR-SEM and tapping mode AFM images of thin films annealed at $600\,^{\circ}\mathrm{C}$ (a-c) and $850\,^{\circ}\mathrm{C}$ (d-f). Image (a) and (d) are HR-SEM top views and image (b) and (e) HR-SEM cross-sectional views. The color scale of the AFM images in (c) and (f) is nonlinear in these cases. (The thin films were made from solution **1** of which pH was adjusted to 9 by adding $25\,\%\ w/w$ aqueous ammonium hydroxide. The film viewed in (e) is different from that shown in image (d) and (f). The sample in (e) was made with a solution to which no pH adjustments were made, containing polymer of $50,000 - 100,000\ \mathrm{g \cdot mol^{-1}}$. This film was spin cast at $1500\ \mathrm{rpm}$ and placed on a hot stage at $120\,^{\circ}\mathrm{C}$.)

The hills and craters observed in Figure 4.1 are randomly dispersed and do not indicate any relation with surface waves. The scenario that protrusions were formed by diffusion is therefore more plausible at least in these cases. This observation does not mean that no convection processes took place during thermal treatment. Particularly in the case of the sample annealed at $600\,^{\circ}\mathrm{C}$, the surface between the hills is roughened as well. Such roughening – which is most clearly observed in image (a) and (c) – may have been driven by flow processes.

4.2 Comparison of the crystallinity of two films annealed at different temperatures

The sharp edges typically found on the hills may indicate crystallinity. Comparison between X-ray diffraction measurements conducted on samples annealed at $600\,^{\circ}\mathrm{C}$ and $850\,^{\circ}\mathrm{C}$ may therefore provide additional information. Both $\omega - 2\theta$ and 2θ measurements on thin films resulting from the standard procedure did however not provide evidence for crystallinity inside these films. The reason may either be because the films were too thin, or because (long-range) symmetry in the films was absent. To produce thicker layers, films were processed by following a different approach.

Changing the procedure

Instead of using a hot stage at $180\,^{\circ}\mathrm{C}$, thin films for XRD measurements were exposed to significantly higher hot stage temperatures of up to $550\,^{\circ}\mathrm{C}$. This way, not only solvent but also organic components were removed directly after spin coating. This process occurred very violently, leaving a thick and low-density film. Multiple layers were spin cast on top of each other before final thermal treatment was applied. The HR-SEM image in Figure 4.2 was for instance obtained by spin casting eight layers, placing the sample on a hot stage at approximately $550\,^{\circ}\mathrm{C}$ between every new coating.

The layers produced by this method contained a substantial larger amount of material than those made by the standard procedure. This difference was not only caused by the fact that more layers were spin cast, but also by the high porosity of the film. Additional material was captured inside the porous network during application of the subsequent coatings.

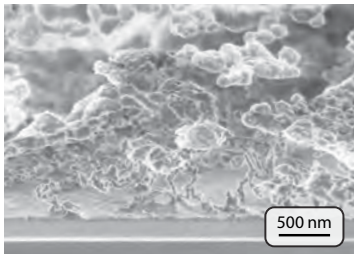

Figure 4.2: Film produced by spin coating eight layers, placing the sample on a hot stage at approximately $550\,^{\circ}\mathrm{C}$ between every coating. The film was finally annealed at $850\,^{\circ}\mathrm{C}$ for two hours.

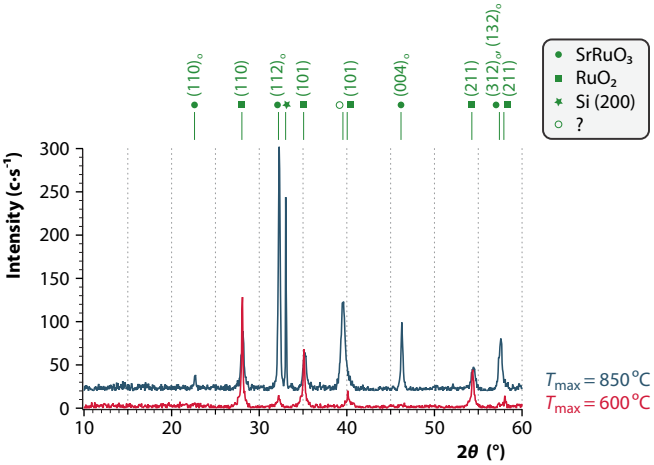

Figure 4.3: XRD spectra of two films annealed at different temperatures. The spectrum that has its baseline at zero intensity (in red) was obtained from a film consisting of ten spin cast layers. Between every coating, the sample was placed on a hot stage at approximately $500\,^{\circ}\mathrm{C}$. The film was finally annealed at $600\,^{\circ}\mathrm{C}$ for three hours. The spectrum that is shifted up by $20\ \mathrm{c}\cdot\mathrm{s}^{-1}$ (in blue) was obtained by casting 17 layers by alternately spin coating a layer and placing the sample on a hot stage at $550\,^{\circ}\mathrm{C}$. This film was annealed at $850\,^{\circ}\mathrm{C}$ for two hours. Both spectra were obtained from $\omega - 2\theta$ scans, with a step size of 0.05° and a counting time of 5 s per step. The insets show the position of diffraction lines of $SrRuO_3$ and RuO_2, based on reference [6] and [54] respectively.

Resulting XRD spectra

The spectra of both a film annealed at $600\,^{\circ}\mathrm{C}$ and a film annealed at $850\,^{\circ}\mathrm{C}$ are presented in Figure 4.3. The spectrum of the film annealed at $850\,^{\circ}\mathrm{C}$ (in blue) was shifted up by $20\ \mathrm{c}\cdot\mathrm{s}^{-1}$. These spectra show that both films are essentially different. The film annealed at $600\,^{\circ}\mathrm{C}$ contained mainly RuO_2 crystals, while the amount of $SrRuO_3$ was negligible. On the contrary, the film annealed at $850\,^{\circ}\mathrm{C}$ contained a considerable fraction of $SrRuO_3$, together with RuO_2. Besides, an unknown peak appeared around $2\theta = 40^{\circ}$.

The film annealed at $600\,^{\circ}\mathrm{C}$ was post-annealed in a pre-heated microwave at $850\,^{\circ}\mathrm{C}$ for one hour. The XRD spectrum that was recorded (not shown) from this film did not show significant differences with that recorded before post-annealing. This observation indicates that at least some of the crystallization processes were characterized by low formation or decomposition rates of $SrRuO_3$ or RuO_2.

Taking a closer look at Figure 4.2 reveals that a thin dense layer was formed on the substrate. This layer will have been attached more firmly to the substrate than the porous layer above. To remove the porous film, the sample annealed at $850\,^{\circ}\mathrm{C}$ was wiped cleaned with a cloth soaked with ethanol. Afterwards, a new XRD spectrum was recorded (not shown). Interestingly, only a small RuO_2 signal remained, indicating that no $SrRuO_3$ was formed near the substrate. The unidentified peak around $2\theta = 40^{\circ}$ was recorded as well, having similar proportions to that recorded in Figure 4.3.

4.3 Studies to the development of RuO_2 and $SrRuO_3$ versus temperature and time

Even more information of the crystallization processes can be obtained if spectra are recorded during annealing. Diffraction from the (110) plane of RuO_2 is expected around $2\theta = 28.0^{\circ}$,[54] and a signal around $2\theta = 32.2^{\circ}$ indicates the presence of $SrRuO_3$ $(112)_o$.[6] These two signals are both the strongest signals for the materials and are relatively close to each other on the 2θ axis. This property facilitates XRD studies to the development of both phases during annealing.

The measuring method

Twenty layers of solution **1** were coated on an oxidized silicon substrate with the hot stage set to $260\,^{\circ}\mathrm{C}$. Without post-annealing, the sample was placed in a D8 discover X-ray diffractomer (Bruker AXS) containing a DHS 900 domed hot stage (Anton Paar). An air flow of approximately $50\ \mathrm{cm}^3 \cdot \mathrm{min}^{-1}$ was guided through this dome.

The temperature inside the domed hot stage was increased to $350\,^{\circ}\mathrm{C}$ at $0.17\,^{\circ}\mathrm{C} \cdot \mathrm{s}^{-1}$. After reaching this temperature, measurements were conducted by changing 2θ from 27.00° to 34.00° with a step size of 0.05° and fixed ω of 5°. After measuring at $350\,^{\circ}\mathrm{C}$, the temperature was further increased to $400\,^{\circ}\mathrm{C}$ and new measurements were started. This way, twelve spectra were measured up to a temperature of $850\,^{\circ}\mathrm{C}$, according to the procedure summarized in Table 4.1. Variables that are not mentioned in this table, were unchanged with regard to those mentioned for measurements conducted at $350\,^{\circ}\mathrm{C}$.

After the measurements at $850\,^{\circ}\mathrm{C}$ were finished, the temperature of the hot stage was allowed to decrease to $50\,^{\circ}\mathrm{C}$ at a maximum rate of $0.17\,^{\circ}\mathrm{C} \cdot \mathrm{s}^{-1}$. When this temperature was reached, XRD measurements were conducted on the film again. The result of these measurements are termed α. The sample was removed from the X-ray diffractometer and placed in the laboratory chamber furnace at room temperature that was heated to $850\,^{\circ}\mathrm{C}$ at $4\,^{\circ}\mathrm{C} \cdot \mathrm{min}^{-1}$. The furnace was kept at this temperature for ten hours, after which it was allowed to cool to room temperature. The sample was subsequently replaced in the X-ray diffractometer and a new measurement was conducted at room temperature. The result of this measurement will be referred to as β.

Analyzing the results

Resulting spectra are included in a box plot in Figure 4.4(a). The spectra are colored red between $2\theta = 27.0^{\circ}$ and 28.5° and blue between $2\theta = 31.0^{\circ}$ and 33.0°. Signals in the red parts are caused by presence of RuO_2 crystallites, while the presence of $SrRuO_3$ is demonstrated by signals in the blue parts. The remainder of the spectrum is colored green and is considered noise.

Mean noise intensities were determined for every spectrum individually and subtracted from these spectra. Thereupon, areas under the red and blue curves were determined using the trapezoidal rule of Riemann summation. The areas that result from Riemann summation are indications of the amount of a certain phase. The data resulting from these approximations are plotted in Figure 4.4(b).

The RuO_2 data in Figure 4.4(b) can be divided into two regions: a region in which the amount of RuO_2 grows or remains unchanged and a region in which RuO_2 decomposes. The data of the first region was fitted with the Hill equation while the data of the latter region was approximated by a linear curve. The $SrRuO_3$ data was fitted by just the Hill equation. The Hill equation is given in Equation 4.1.

Temperature range ($^{\circ}\mathrm{C}$)	**Temperature change between measurements** ($^{\circ}\mathrm{C}$)	**Measurement time** ($\mathrm{s} \cdot \mathrm{step}^{-1}$)	**Label**
$350 - 450$	50	15	-
$475 - 500$	25	10	-
$550 - 850$	50	7	-
50	-	20	α
27	-	20	β

Table 4.1: Measuring program to study the development of phases in temperature and time.

$$y = base + \frac{max - base}{1 + (\frac{x_{1/2}}{x})^{rate}} \tag{4.1}$$

$base$: y value at $x = -\infty$
max: y value at $x = \infty$
$x_{1/2}$: x at $y = \frac{base+max}{2}$
$rate$: rise rate

The development of RuO_2 and $SrRuO_3$

The results show that RuO_2 had formed between $350\,^{\circ}\mathrm{C}$ and $400\,^{\circ}\mathrm{C}$, while $SrRuO_3$ started to form at a significantly higher temperature of about $600\,^{\circ}\mathrm{C}$. The TGA results in Figure 2.4 indicate that RuO_2 developed during decomposition of organics while $SrRuO_3$ formed well after the main decomposition processes had finished. Besides, the formation of RuO_2 proceeded at a higher rate than the formation of $SrRuO_3$. Both phases stopped growing after a certain amount of phase had formed.

Previously, exothermic peaks in the DSC signal of Figure 2.4 were related to crystallization processes. A peak at $346\,^{\circ}\mathrm{C}$ was related to the formation of RuO_2, and a peak at $845\,^{\circ}\mathrm{C}$ to the formation of $SrRuO_3$. The first peak coincides well with the results of Figure 4.4, but the latter does not. The average heating rate during the combined TGA and DSC measurements was higher than that of the XRD measurements. $SrRuO_3$ may have formed at a higher temperature during the TGA/DSC measurements, because the formation of this material is limited by slow kinetics.

The areas below the peaks of both RuO_2 and $SrRuO_3$ reach a maximum of $14\ \mathrm{c}\cdot^{\circ}\cdot\mathrm{s}^{-1}$. These signals are in both cases the strongest signals for the phases. For this reason, weight percentages of RuO_2 and $SrRuO_3$ can be estimated by using relative intensity ratio (RIR) values. RIR values give the intensity of a specific phase with regard to that of corundum when both phases would be mixed in a one-to-one weight ratio. The RIR values found for RuO_2 and $SrRuO_3$ are 7.75 en 8.00 respectively.[6,54] Based on the chemical amount of the two phases, significantly more RuO_2 than $SrRuO_3$ had probably developed during the experiments.

Preliminary formation of RuO_2 was observed in other CSD approaches to make $SrRuO_3$.[e.g. 14,16,17] RuO_2 can even be obtained from sol-gel routes at temperatures below $300\,^{\circ}\mathrm{C}$.[55] These observations form additional evidence that the energy barrier for the formation of RuO_2 is lower than that for the formation of $SrRuO_3$ at low temperatures.

RuO_2 disappeared after a temperature of approximately $600\,^{\circ}\mathrm{C}$ was reached. The amount of decomposed phase seemed to increase linearly with increasing temperature. The results indicated with α and β though, show that the linear trend observed is not related to a temperature dependent equilibrium.

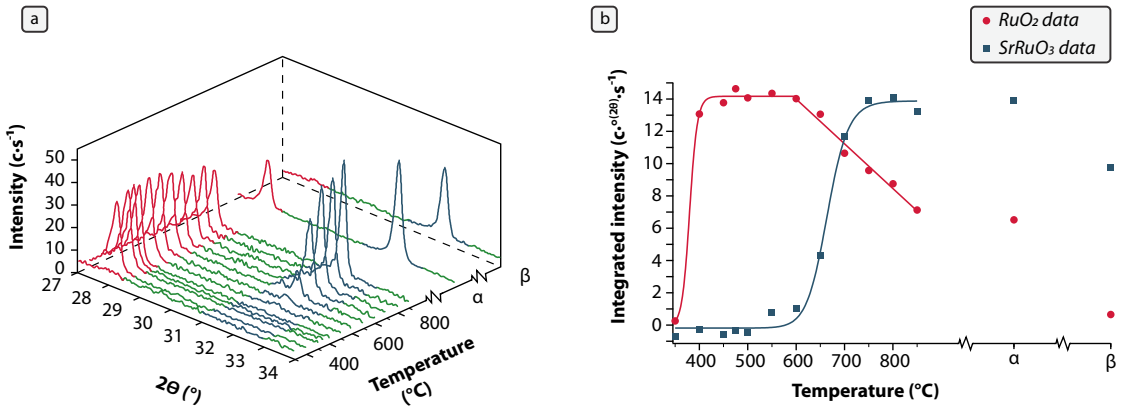

Figure 4.4: Figure (a) shows X-ray diffraction spectra measured between $2\theta = 27 - 34^{\circ}$ as a function of the annealing temperature. Curves between $2\theta = 27.0^{\circ}$ and 28.5° indicate the presence of RuO_2 (red), while curves between $2\theta = 31.0^{\circ}$ and 33.0° indicate the presence of $SrRuO_3$ (blue). The areas under these curves were determined and plotted in figure (b). The captions α and β on the temperature axes are explained in the text of Section 4.3.

Although RuO_2 started to disintegrate at the moment $SrRuO_3$ started to form, at least a considerable part of the RuO_2 phase was not included in the $SrRuO_3$ phase during disintegration. After all, between $750\,^{\circ}C$ and $850\,^{\circ}C$ RuO_2 was still disappearing while the amount of $SrRuO_3$ remained unchanged. The disappearing of crystalline RuO_2 can therefore not be simply explained by a transition to $SrRuO_3$.

4.4 The development of phases in thin films

Based on the XRD results, it seems plausible to believe that the hills observed in Figure 4.1(a-c) are composed of RuO_2. The film in these images was annealed at $600\,^{\circ}C$, at which RuO_2 was measured to be the persistent phase. These measurements were based on thicker films though, that had been formed by a different procedure. The assumption was taken as being true, since XRD measurements on the single layer thin films that were annealed to $850\,^{\circ}C$, did not expose any reasonable peaks. However, final XRD measurements on thin films annealed at $600\,^{\circ}C$ revealed that the assumption is incorrect.

A spectrum that was obtained from $\omega - 2\theta$ measurements on such a film is presented in Figure 4.5. Apart from the annealing temperature, this film was made according to the standard procedure. The three strongest peaks of $SrRuO_3$ can be identified in the spectrum, whereas no peaks stemming from RuO_2 appeared. The initial assumption that hills consist of RuO_2 was rejected, since it is now believed that the hills may actually consist of $SrRuO_3$.

The reason why $SrRuO_3$ was detected in this case is supposed to be related to the thickness of the film. The films from the standard procedure were significantly thinner than those made specifically for XRD measurements. Bulk nucleation may have determined the crystallization in the thick and porous films, whereas interface nucleation may have dominated in the thin films. Generally, the energy barrier of interface nucleation is lower than that of bulk nucleation. The difference in barrier heights depend on *e.g.* the surface energy[25] and will thus differ for RuO_2 and $SrRuO_3$. It might be that the energy barrier for heterogeneous nucleation of $SrRuO_3$ is lower than that of RuO_2, while it is higher for homogeneous nucleation. However, the cause remains a matter of conjecture.

4.5 Studies on the composition of thin films

Volatilization of Ru at temperatures exceeding $600\,^{\circ}C$ forms a plausible explanation for the disintegration that is observed in the XRD spectra. In order to investigate whether ruthenium species could have migrated into the gas phase, EDX and XPS measurements were conducted on selected films.

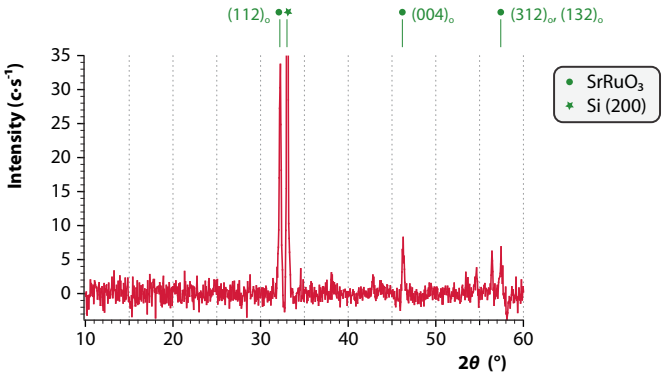

Figure 4.5: XRD spectrum of a film that was made according to the standard procedure, with the exception that it was annealed at $600\,^{\circ}C$. The spectrum was recorded in $\omega - 2\theta$ mode with a step size of 0.05° and a counting time of 20 seconds per step applied.

EDX analysis

The films that are shown in Figure 4.1(a) and (d) were both analyzed by EDX. Measurements were conducted at different positions on these films. Measurements on the film of Figure 4.1(d) were for instance conducted on a large crater, and on the layer between the craters. Analysis of the X-rays emitted from these samples gave the results as presented in Table 4.2.

Ruthenium was only detected in the hills of the sample annealed at $600\,^{\circ}\mathrm{C}$. The measured absence of this element on the film annealed at $850\,^{\circ}\mathrm{C}$, forms an indication that it had escaped. It might also be that no ruthenium was found because the film thickness was below the measurable limits of EDX. However, the measured carbon contents are in contradiction with this hypothesis.

The higher oxygen content measured on the hills compared to that measured in the film annealed at $850\,^{\circ}\mathrm{C}$ indicates that the hills contain metal oxides. A higher Sr content was measured on the hills as well. This value can be questioned though, since the energy of the K radiation produced by Si overlaps with the L radiation produced by Sr.

The results further prove that the carbon content in the hills and craters were relatively high. Again, this observation is at odds with allegations made by Burrell and co-workers, who state that decomposition leads to extremely clean thin films. [20]

XPS analysis

EDX collects data mainly from a few nanometers under the surface. To obtain more reliable numbers for the contents of the surface, XPS measurements were conducted. The thin film that was studied by XPS was produced by the standard procedure on a modified oxidized silicon substrate (as discussed in Section 5.2.3). At this point, it is only important to know that the thin film was produced on a modified substrate with an annealing temperature of $850\,^{\circ}\mathrm{C}$.

The results in Table 4.2 show that no ruthenium was present in the thin film, which forms another indication of its volatility. Possible oxidation of this compound into extremely volatile RuO_3 or RuO_4 may form a possible pathway for its volatilization. Also, the increased vapor pressure due to the curved interfaces of the crystallites may contribute to the volatility (as described by the Kelvin equation in 4.2). In contrast to the measured ruthenium content, a considerable amount of carbon was detected.

$$ln\left(\frac{p_{\mathrm{c}}}{p_{\infty}}\right) = \frac{\gamma \cdot V_{\mathrm{m}}}{R \cdot T} \cdot \left(\frac{2}{r_{\mathrm{m}}}\right) \tag{4.2}$$

p: Vapor pressure
γ: surface tension
V_{m}: molar volume
R: gas constant
T: temperature
r_{m}: radius of curvature (of the particle)
c: the curved surface
∞: the flat surface

4.6 Interfacial effects

The material in thin films is in close contact with both the substrate and the atmosphere. Interactions at these interfaces can therefore make a major contribution to the final shape, crystallinity and even composition of thin films. Two important interfacial effects are treated in this section.

Sample	Method	Position scanned	O	Si	C	Ru	Sr
			atomic concentration (%)				
a	EDX	On a hill	61.7	24.0	8.1	3.4	2.8
b	EDX	On a crater	44.8	45.0	9.5	0.1	0.7
b	EDX	On the smooth area between craters	47.5	51.2	0.7	0.1	0.6
c	XPS	On the middle of the film	58.3	15.4	11.9	0.0	14.4

Table 4.2: Summary of EDX and XPS results for three different films. Sample *a* was annealed at $600\,^{\circ}\mathrm{C}$ and is the same as shown in Figure 4.1(a-c). Sample *b* was annealed at $850\,^{\circ}\mathrm{C}$ and is shown in Figure 4.1(d). The XPS results of sample *c* concern a survey spectrum scan made with an X-ray beam of $100\ \mu\mathrm{m}$ in diameter. This sample was produced by first spin coating and annealing a Sr precursor solution before spin coating the SRO solution as described in Section 5.2.3.

4.6.1 Processes occurring at the substrate interface

Though previous AFM images give an idea of the shape of films that are formed on oxidized silicon, additional information can be obtained from cross-sectional HR-SEM images, as the one in Figure 4.6. The film shown in this figure was estimated to vary in thickness between 15 and $50\ \mathrm{nm}$. The interface between the substrate and film does not follow a straight line. For this reason, interdiffusion processes are believed to have taken place between species in the substrate and the thin film.

Alkaline and alkaline earth metals are known to be prone to diffuse into glasses, disrupting the Si-O network. Strontium falls in the group of alkaline earth metals and – as such – is classified as a glass network modifier. Diffusion of Sr^{2+} may took place during thermal treatment, explaining the unsharp interfaces observed in HR-SEM images. The material inside these regions is expected to exhibit some degree of crystallinity, since restructuring of the atoms is facilitated in the disrupted network.[56,57] However, no induced crystallinity was observed after $\omega - 2\theta$ measurements on a film that was made with just the strontium precursor solution.

4.6.2 The influence of water vapor

In the following chapter, the considerable influence of water vapor on the film forming process during removal of the polymer is demonstrated by Bénard cells. Humidity is believed to be a major contributor also to the low reproducibility of the thin films presented in the previous chapter. The reason is that water may catalyze the depolymerization reaction of the polymer. The mechanism behind this reaction is given in Figure 4.7.

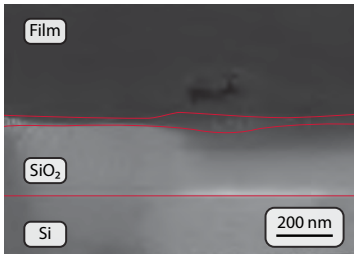

Figure 4.6: Cross-sectional HR-SEM image of a thin film on oxidized silicon. The interfaces are highlighted by red lines. (The sample was made by a precursor solution containing polymer of $50,000 - 100,000\ \mathrm{g \cdot mol^{-1}}$, that was spin cast at $1500\ \mathrm{rpm}$.)

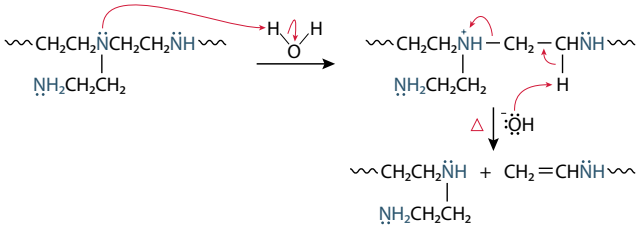

Figure 4.7: Mechanism behind the depolymerization of polyethyleneimine, catalyzed by water.

Chapter 5

Controlling thin film growth

In the previous chapter, different processes are described that are expected to influence the film forming process. A following step is to use this information and evaluate possible measures that may lead to films of increased quality. Films are considered to be of high quality if they are dense, smooth, and crystalline. Several approaches were evaluated with the goal to increase the quality of films with regard to films produced by the standard method. The results of these approaches are discussed in this chapter.

Since film roughening mainly proceeds during thermal treatment, an obvious starting point to fight roughening is by introducing and evaluating changes made at this final stage. Various one and two-step thermal treatment methods were evaluated and are discussed in the first section. Also the stages before thermal treatment can be adjusted to control the nature of final films. Subsequent sections treat the influence of the substrate and the solution on the quality of annealed films.

5.1 Changing the thermal treatment

5.1.1 One-step processing

Microwave annealing The formation of hills (that were observed in the samples annealed at $600\,^{\circ}\mathrm{C}$) may have been facilitated by simultaneous decomposition of the organic components. The viscosity of the film at this stage will be influenced considerably by the rate at which organics are removed. For this reason, the effects of rapid thermal annealing were investigated.

Fast firing experiments were effected in a MicroSYNTH Labstation (Milestone) by two approaches. In a first approach, a sample was placed in the microwave furnace that contained sample crucibles pre-heated to $850\,^{\circ}\mathrm{C}$. This temperature was maintained for 72 minutes, after which the microwave furnace was allowed to cool to room temperature.

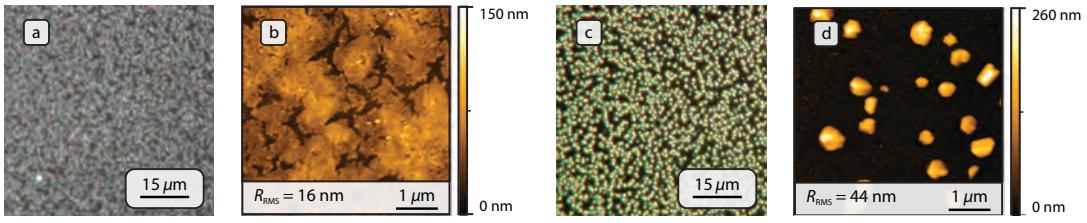

Figure 5.1: Dark field optical microscopy and tapping mode AFM images of films annealed in a microwave furnace in a single step. The thin film in image (a) and (b) was obtained by placing it in a pre-heated microwave furnace at $850\,^{\circ}\mathrm{C}$ for 72 minutes. Image (c) and (d) show a thin film that was obtained by placing a sample in a microwave furnace at room temperature that was subsequently heated to $850\,^{\circ}\mathrm{C}$. The temperature was reached within 11 minutes by heating with $1000\ \mathrm{W}$, and was maintained for 61 minutes.

In a second approach, a sample was placed in the microwave furnace that was at room temperature. Heating with $1000\ \mathrm{W}$ was subsequently applied until the sample crucibles reached a temperature of $850\,^{\circ}\mathrm{C}$. This took approximately 11 minutes. The crucibles were kept at this temperature for an hour, after which they were allowed to cool to room temperature.

The topography of the films was analyzed by optical microscopy and AFM. The images are given in Figure 5.1. Image (a) and (b) show the film that resulted from the first approach. In the second approach, a film was formed that is shown in (c) and (d). The films were furthermore studied by XRD 2θ measurements (not shown). No crystallinity was observed on the film that was annealed in a pre-heated microwave furnace. Conversely, indications of $SrRuO_3$ were found on the sample produced by the other approach. The signal was very weak though, since the strongest peak – corresponding to diffraction from the $(112)_o$ plane – did not exceed $4\ \mathrm{c}\cdot\mathrm{s}^{-1}$.

The film that was annealed in a pre-heated microwave furnace did clearly have a different topography from the samples studied previously. The thickness of this film is not constant, and cracks are observed on the thinner parts. This demonstrates the high rate at which organics were removed during the process, leaving a film of low density. Free diffusion of the precursor species will have been limited during this vigorous process, which may explain why no crystalline material was detected. Clearly, this approach did not yield films of the desired quality.

Hills are seen on the film that was annealed by starting with a microwave furnace at room temperature. These hills – with their sharp edges – look similar to those observed in Figure 4.1(a-c). The fact that XRD gave indications for the presence of $SrRuO_3$ indicates that these hills were composed of this phase. If these hills are indeed similar to those observed previously, it is remarkable that the hills were observed after annealing to a temperature at which they are believed to be unstable. This observation may be explained by assuming that the formation of these hills took place during the first minutes, before the annealing temperature was reached. Subsequent decomposition had then proceeded gradually such that it was unfinished after the complete annealing. No matter what the explanation for the formation of these hills is, clearly this kind of topography is undesired. Therefore, rapid thermal annealing is not the solution to increase the quality of thin films.

Annealing in a confined space

Some of the films were covered with a porcelain boat ($45\times25\times10\ \mathrm{mm}^3$) during annealing in the chamber furnace. The reason to do so was that it was believed that the evaporation of ruthenium could be suppressed or reduced in a confined space. Besides, the covering of the films was expected to influence the decomposition behavior of the organics because exhaust gasses could not easily escape.

The experiments were conducted in different ways. In one particular case, two thin films were annealed simultaneously under the same porcelain boat. Analysis of one of these films gave the images given in Figure 5.2 (a) and (b). Another thin film was produced by a slightly different approach: only one thin film was spin cast and placed under the boat. An amount of $200\ \mu\mathrm{l}$ of the solution was placed on a different substrate and without spin coating, the solvent was removed on a hot stage. This substrate was also placed under the boat. Resulting images of the spin cast film are presented in image (c) and (d).

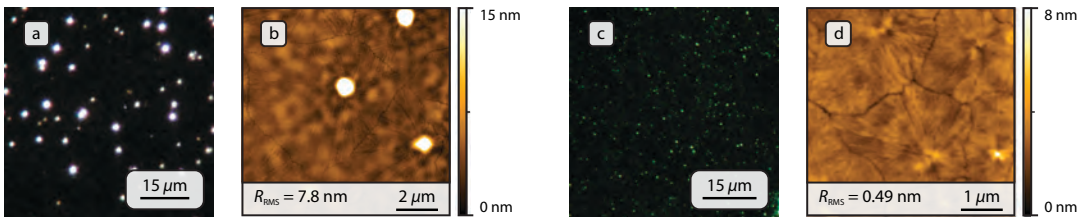

Figure 5.2: Dark field optical microscopy and tapping mode AFM images showing two films annealed at $850\,^{\circ}\mathrm{C}$ under a porcelain boat ($45\times25\times10\ mm^3$). Further details are given in the accompanying text. (The thin film in image (c) and (d) was made with solution **1** of which pH was adjusted to 8.5 with a $25\,\%\ w/w$ aqueous ammonium hydroxide solution. During spin coating, this sample was accelerated with $220\ \mathrm{rpm}\cdot\mathrm{s}^{-1}$. Also, a heating rate of $0.5\,^{\circ}\mathrm{C}\cdot\mathrm{min}^{-1}$ was applied between 200 and $400\,^{\circ}\mathrm{C}$.)

The thin films produced were dissimilar to those treated previously. In both cases, the films are characterized by having protrusions which are surrounded by cracks. If a line is drawn between two protrusions, the cracks are situated at the middle of this line and are aligned perpendicular. The film rupture observed at these places is believed to be a result of interfacial effects between the protrusions and the decomposing thin film.

Having a root mean square roughness below $1\ \mathrm{nm}$, the film in image (c,d) is extremely smooth. On the other hand, protrusions that can reach up to $200\ \mathrm{nm}$ were detected on the other film. These considerable differences are believed to be related to the gas phase composition during the decomposition of organics. In another experiment, a droplet of PEI was placed on a separate substrate and placed under a porcelain boat. A thin film – spin cast by the standard procedure – was placed under this boat as well. After annealing at $600\,^{\circ}\mathrm{C}$, clear differences were observed between two sides of the thin film (not shown). At one side, large protrusions were observed while smaller but significantly more concentrated protrusions were formed on the other side. The partial pressure of ethenamine may determine the depolymerization process to a large extent. The effect is believed to be comparable to that of water vapor: the amine groups in ethenamine may catalyze the depolymerization process.

Although smooth films can be formed by following this approach, obtaining films of the desired composition and good crystalline quality may still be challenging. XRD measurements on some of the films did not indicate the presence of $SrRuO_3$. Furthermore, the layers were found insulating according to measurements with a digital multimeter (Peaktech). It is well conceivable that ruthenium exists as the tetraoxide in the gas phase, which may not be reduced at the processing temperature. Thermodynamic studies revealed that the gas phase reduction of RuO_4 can only proceed spontaneously at temperatures exceeding $1425\,^{\circ}\mathrm{C}$.[58]

5.1.2 Two-step processing

Removal of organics below the crystallization temperature In the standard procedure, removal of the organics and crystallization is effected in a single step. The formation of hills is believed to be a crystallization process that is facilitated by considerable diffusion lengths of precursor species. These large diffusion lengths are the result of the considerable reduction in the viscosity of the film during the depolymerization process. Thus, if the removal of the organic components and crystallization can be separated into different steps, the formation of hills may be prevented or their dimensions reduced.

In one approach, the organics were partly removed by slowly heating the films in air up to a temperature below the expected crystallization temperature. This step was conducted in an open tube furnace (RS 80/300/11 provided by Nabertherm) that was heated to $325\,^{\circ}\mathrm{C}$ at $30\,^{\circ}\mathrm{C}\cdot\mathrm{h}^{-1}$. After reaching the desired temperature, it was kept for four hours.

In the following step, the remainders of the organic components were removed and crystallization was intended. This step was performed in a pre-heated microwave furnace. The applied annealing temperature ranged from $600\,^{\circ}\mathrm{C}$ to $850\,^{\circ}\mathrm{C}$. Films were always annealed for 72 minutes.

The result of the first thermal treatment step is given by the AFM height image of figure 5.3(a). No significant protrusions could be detected on this films. The slight film roughening is believed to be caused by the concentration differences that were created during the decomposition of organics.

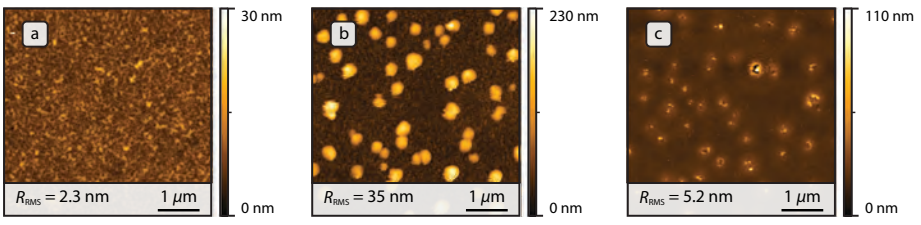

Figure 5.3: Tapping mode AFM images showing a film after different stages of a two-step thermal treatment. Image (a) shows the film directly after the first thermal treatment step that was conducted in an open tube furnace at $325\,^{\circ}\mathrm{C}$. The film was subsequently placed in a pre-heated microwave furnace at $650\,^{\circ}\mathrm{C}$, in which the temperature was maintained for 72 minutes. The resulting thin film is depicted in image (b). In a post-annealing step, the sample was kept in a chamber furnace at $850\,^{\circ}\mathrm{C}$ ($4\,^{\circ}\mathrm{C}\cdot\mathrm{min}^{-1}$) for ten hours, resulting in the thin film shown in (c).

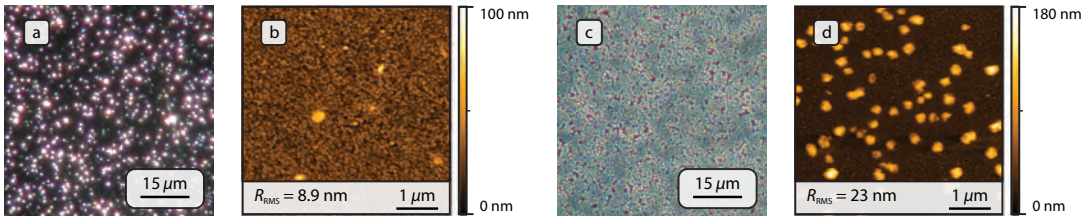

Figure 5.4: Dark field optical microscopy and AFM images showing two films – in (a,b) and (c,d) – that were produced under the same conditions in a two-step thermal treatment procedure. The films were produced apart from each other with solutions of a few hours old. The first annealing step was conducted in air at $325\,^{\circ}\mathrm{C}$. The second annealing step was effected in a pre-heated microwave furnace at $850\,^{\circ}\mathrm{C}$. Although the entire procedure was the same, the resulting films clearly differ considerable in *e.g.* roughness. This illustrates the poor reproducibility of this method.

The AFM image in Figure 5.3(b) shows that hills had developed during the second thermal treatment stage. The particular image shows the result of annealing at $650\,^{\circ}\mathrm{C}$, but films of similar topography were obtained after annealing at different temperatures (see *e.g.* Figure 5.4). After post-annealing the film in a chamber furnace at $850\,^{\circ}\mathrm{C}$ for ten hours, the hills had disappeared. Presence of $SrRuO_3$ was indicated by XRD measurements (not shown) on a film annealed at $600\,^{\circ}\mathrm{C}$, but not on the film that was post-annealed. This forms another indication to suspect that the hills were composed of $SrRuO_3$.

This method does not yield the desired thin films and besides the reproducibility is poor. The two films shown in Figure 5.4 are clearly different but were created following equal procedures. The critical step is believed to be the insertion of samples in the pre-heated microwave furnace. During the first seconds after the insertion, the film rapidly heats up to the annealing temperature. Supposedly, small differences in how the samples are inserted can make large differences on the final topography.

It may as well be that the final topography – that is formed during the second thermal treatment step – will already be determined during the first step. Sulphur pollution on thin films annealed in different tube furnaces was found by both XPS and EDX measurements. Such pollution may have an effect on the development of thin films.

Removal of organics in nitrogen gas atmosphere

In different attempts, organics were removed in a stream of pure nitrogen gas. The primary reason to remove the organics in a nitrogen atmosphere was to hamper crystallization by the exclusion of atmospheric oxygen. The expectations were that more of the organic constituents could be removed by increasing the annealing temperature, without effecting (significant) crystallization events.

The first thermal treatment step was conducted in the tube furnace, through which a nitrogen gas flow of $80\ \mathrm{ml}\cdot\mathrm{min}^{-1}$ was guided. The outlet of this furnace (having an inner diameter of $5\ \mathrm{cm}$) was covered with a piece of aluminum foil in which five holes were pierced with a cocktail stick. Various results proved the importance of covering the outlet in order to gain a desired gas composition near the film. For the same reason, the temperature program was started after the furnace was

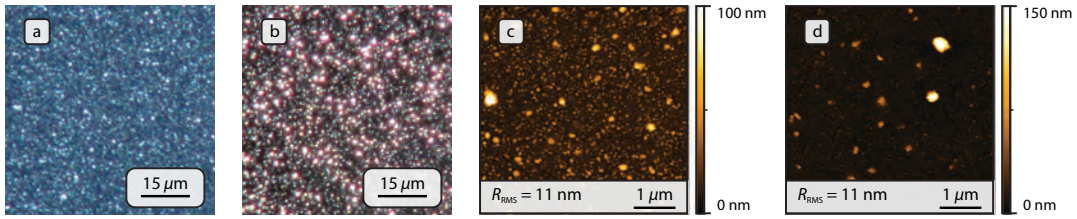

Figure 5.5: Thin films that were thermally treated according to a two-step procedure, in which the first step was effected in a nitrogen gas stream. Image (a) and (b) show dark field optical microscopy images of a thin film respectively before and after the second step in the thermal treatment. Image (c) and (d) are tapping mode AFM height images of two different thin films. The film in image (c) – which is equal to that in (b) – was heated in the first step at $50\,^{\circ}\mathrm{C}\cdot\mathrm{min}^{-1}$; the film in (d) was heated at $240\,^{\circ}\mathrm{C}\cdot\mathrm{min}^{-1}$.

flushed for two hours with the gas stream. Different temperature programs were used, in which the furnace temperature was increased to $500\,^{\circ}\mathrm{C}$ at heating rates between 0.5 and $4\,^{\circ}\mathrm{C}\cdot\mathrm{min}^{-1}$. After the furnace was held at the annealing temperature for 10 minutes, it was allowed to cool down to room temperature. The second annealing step was performed in the microwave furnace, which was pre-heated to $850\,^{\circ}\mathrm{C}$. Maximum four samples per run were kept at this temperature for 72 minutes.

Dark field optical microscopy images of the film before and after the second annealing step are presented in Figure 5.5(a) and (b) respectively. The film was roughened after the first thermal treatment step, but protrusions clearly grew during annealing in the microwave furnace. The AFM image in (c) – which was produced after the second thermal treatment step – shows that protrusions are situated everywhere over the film. Although still not ideal, the film was of better topographical quality. No peaks were observed in XRD results though (not after $\omega - 2\theta$ and nor after 2θ scans).

Films were also made with higher heating rates applied in the first step of the thermal treatment. These films were of similar topography. Figure 5.5(d) for example shows an AFM image of a sample that was heated to $500\,^{\circ}\mathrm{C}$ with an almost 5 times higher heating rate applied compared to the film shown in image (c).

Removal of organics in forming gas atmosphere

Although crystallization is believed to be hindered in a nitrogen atmosphere, crystallization processes may still take place during removal of the organics. The reason is that oxygen may also be provided by the oxidized silicon substrate or decomposing EDTA molecules. Therefore, the films made in nitrogen atmospheres were also prepared in forming gas (N_2 containing $4\%\ v/v$ H_2).

The reducing property of H_2 may inhibit any crystallization processes. For example RuO_2 is easily reduced to metallic ruthenium according to the reaction: $RuO_2 + 2\,H_2 \longrightarrow Ru + 2\,H_2O$. Whether such reactions can proceed depends on the temperature and partial pressure of the H_2 gas. RuO_2 will *e.g.* be reduced in 1% H_2 in N_2 already at $150\,^{\circ}\mathrm{C}$.[59] Also $SrRuO_3$ can reduce in oxidizing atmospheres into a microcrystalline mixture of metallic Ru, water and SrO.[2]

AFM and optical microscopy images of thin films after the second thermal treatment stage are given in Figure 5.6. The AFM image in (a) shows a completely different topography compared to the images treated before. A maze of material is protruding from the layer beneath. This kind of topography might have developed due to unbalanced tensions in the film by processes similar to those causing Bénard cell formation. Generated water in reduction processes may have caused the tensions to become unbalanced.

The optical microscopy images in Figure 5.6(b) and (c) show films after the second thermal treatment, of which organics had been removed at different rates in a first step. Image (b) was obtained from a film that was heated to the annealing temperature at $50\,^{\circ}\mathrm{C}\cdot\mathrm{h}^{-1}$, and image (c) from a film that was heated at $240\,^{\circ}\mathrm{C}\cdot\mathrm{h}^{-1}$. The film that was heated more rapidly did contain large protrusions, showing that low heating rates in the first step are beneficial for the quality of the films. The fact that these protrusions are observed may indicate better diffusion, that is also expected in the film that decomposed at a higher rate.

Two films formed by this approach were studied by 2θ XRD measurements (not shown). Though very weak, broad peaks were observed at the positions of the two strongest RuO_2 peaks. Presumably,

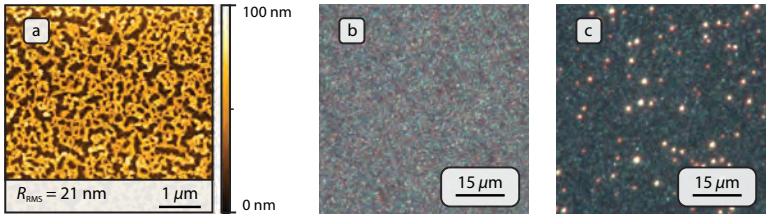

Figure 5.6: Thin films that were thermally treated in two steps, of which the first was effected in a forming gas stream. The dark field optical microscopy pictures in (b) and (c) show thin films annealed in forming gas at $500\,^{\circ}\mathrm{C}$ with heating rates of respectively $50\,^{\circ}\mathrm{C}\cdot\mathrm{h}^{-1}$ and $240\,^{\circ}\mathrm{C}\cdot\mathrm{h}^{-1}$ applied. Image (a) shows a tapping mode AFM image of the film in (b).

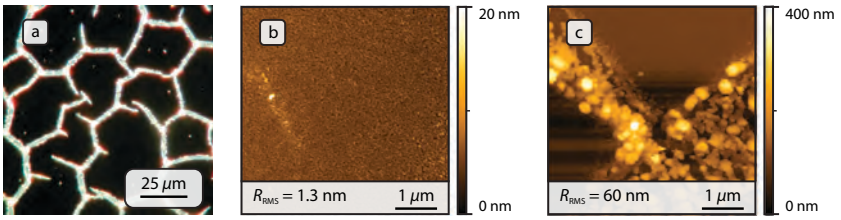

Figure 5.7: Image (a) contains a dark field optical microscopy image showing cellular patterns that were typically encountered when annealing was performed in humid atmospheres. Image (b) and (c) respectively show tapping mode AFM images of the inner part of a cell and the cell edges. The sample shown in this image was produced by annealing a film to $350\,^{\circ}\mathrm{C}$ for six hours at $0.5\,^{\circ}\mathrm{C}\cdot\mathrm{min}^{-1}$ in a stream of forming gas that was led through water.

the undesired RuO_2 phase formed during the annealing process. This might be explained by a different nature of the precursor species, that may have been reduced by H_2. The uncertainty about whether the desired phase had formed, and the considerable roughness measured on the films, seem to also make this procedure unsuitable for the formation of $SrRuO_3$ thin films.

Removal of organics in gas flows bubbled through water

Prior to entering the tube furnace, the gasses were in some cases guided through a bubbler containing water. That this did not lead to smooth films can be observed in Figure 5.7. Although these images particularly show a film that was annealed in forming gas at $350\,^{\circ}\mathrm{C}$, similar patterns were observed on samples that were annealed at a higher temperature or in 'pure' nitrogen gas. The patterns had formed during the first annealing step.

The reason why such patterns are formed in humid atmospheres may be attributed to the catalytic action of water in the depolymerization process of the polymer. Since water molecules are mainly situated at the interface between the film and gas, depolymerization will mainly proceed at the surface and a concentration gradient develops in the direction perpendicular to the film surface. The tensions in the film become unbalanced and convection in the direction of the higher tension regions on the surface will commence (Marangoni convection). This flow pattern may further be enhanced by a temperature gradient (buoyancy driven) developed due to the (endothermic) evaporation or decomposition processes taking place near the film surface.

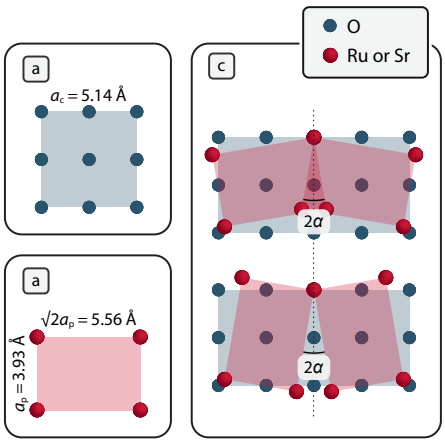

Figure 5.8: Representations of the (100) plane of cubic yttria stabilized zirconia (a), and the $(110)_p$ plane of $SrRuO_3$ (b). These plates can stack by a diagonal rectangle-on-cube principle as represented in (c), in which $\alpha = 9.75^{\circ}$.

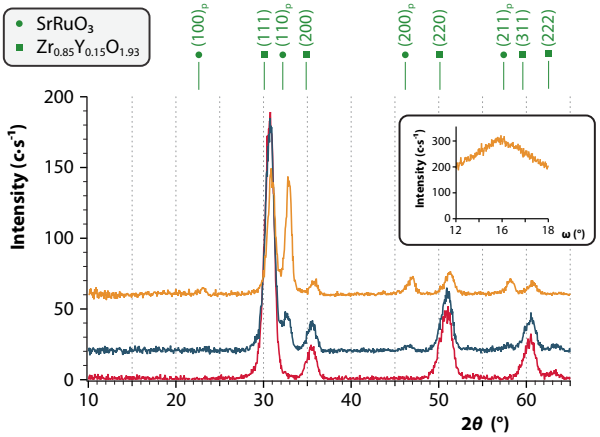

Figure 5.9: 2θ XRD spectra of different layers of $SrRuO_3$ on YSZ. The spectrum that has its baseline at zero intensity (in red) is that of the polycrystalline YSZ substrate. The spectrum that is shifted up by $20\ \mathrm{c}\cdot\mathrm{s}^{-1}$ (in blue) was obtained by scanning a sample on which a first layer was deposited. After casting the seventh layer on this sample, the final spectrum (in orange; shifted up by $60\ \mathrm{c}\cdot\mathrm{s}^{-1}$) was obtained. The diffraction line positions of SRO and YSZ given above the spectra are based on reference [6] and [60] respectively. The Miller indices for the planes of SRO were converted to that of the pseudo-cubic lattice. The inset shows a rocking curve made on the seven layered sample at $2\theta = 32.4^{\circ}$ with a step size of 0.03° measuring $3\ \mathrm{s}\cdot\mathrm{step}^{-1}$.

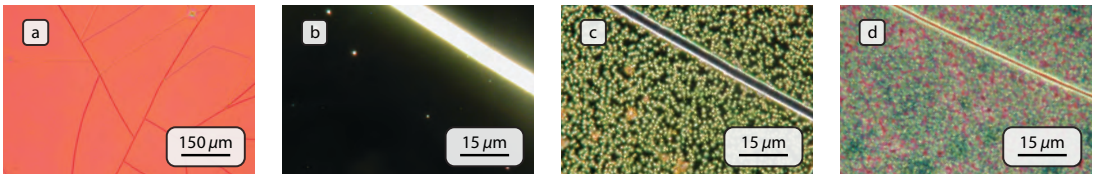

Figure 5.10: Optical microscopy images of a polycrystalline YSZ layer containing a different number of spin cast SRO layers. Image (a) and (b) respectively show a bright field $5\times$ and a dark field $50\times$ magnification of the YSZ film. Image (c) and (d) show dark field $50\times$ magnifications of respectively one and six spin cast SRO layers.

5.2 Changing the substrate

5.2.1 Films on polycrystalline YSZ substrates

Polymer-assisted deposition has been used mainly to form hetero-epitaxial thin films. Its strength therefore seems to lie within epitaxial growth processes. Burrell *et al.* describe polymer-assisted deposition as a bottom-up growth process in which *"the influence of the lattice is emphasized to the extreme"*.[20]

Epitaxial growth of SRO on YSZ is possible, but does not proceed by simple 45° cube-on-cube stacking of $(100)_{\mathrm{p}}$ SRO on (100) YSZ. The compressive strain that would be induced by the mismatch of $8.1\,\%$ is believed to be too large. Instead, SRO can grow with the $(110)_{\mathrm{p}}$ plane parallel to the (100) plane of the substrate. Rectangle-on-cube epitaxy is possible by orientation of the SRO plane by $\pm 9.75^{\circ}$ relatively to the [010] and [001] directions on the substrate. These four degenerate conformations are visualized in Figure 5.8. The mismatch of this conformation is $-6.3\,\%$.[61,62]

YSZ substrates were prepared on boron doped p-type CZ-silicon (001) wafers (Okmetic) by sol-gel deposition. Optical microscopy images of one such substrate are shown in Figure 5.10(a) and (b). Outside of the cracks, these films were extremely smooth ($R_{\mathrm{RMS}} = 0.5$ nm). The substrate was inspected by XRD and showed to be of polycrystalline nature. Thus, only small parts of the substrate could function as a template for the growth of SRO.

The standard procedure was followed to create thin films on the substrates. The only change made was that films were annealed at $700\,^{\circ}\mathrm{C}$ for one hour in the chamber furnace. Eventually seven layers had been spin cast on one substrate by continuously repeating this procedure.

Glancing incidence XRD spectra of the substrate, one spin cast layer, and seven spin cast layers are given in Figure 5.9. These spectra clearly show the development of an $SrRuO_3$ phase on the substrate. No signs of other phases were detected in these spectra. The fact that an SRO phase was detected with the 2θ scan mode, indicates that the phase had little or no texture. To find out whether the layer had any preferred orientation with respect to the substrate surface, a rocking curve was recorded at $2\theta = 32.4^{\circ}$. The blunt curve – as shown in the inset of Figure 5.9 – indicates that the SRO $(100)_{\mathrm{p}}$ plane was not preferentially aligned parallel to the substrate surface.

Both the YSZ and SRO spectra are shifted to higher angles. The fact that similar shifts were observed in $\omega - 2\theta$ scans while the position of the Si(004) peak had not shifted proves that the lattices were indeed compressed compared to literature values. As a matter of fact the measured shifts are small, since the corresponding spacing between planes differs only a few ångströms with the indexed unit cells.

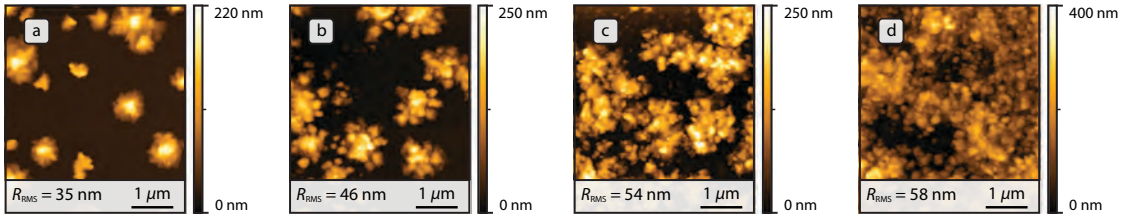

Figure 5.11: Tapping mode AFM height images of respectively one, two, four, and seven spin cast $SrRuO_3$ layers on YSZ.

The topography of the films is revealed by the optical microscopy and AFM height images of Figure 5.10 and 5.11, respectively. The AFM images show that no smooth layer, but islands were formed. These islands grew and coalesced when more layers were deposited. Islands were formed probably because the barrier for (interface) nucleation will have been higher than that for crystal growth. This explanation was also used to explain the origin of hills on oxidized silicon substrates. However, in the latter case a continuous film was observed as well. An explanation for this difference may be that diffusion of Sr^{2+} did occur in the oxidized silicon substrates. Due to this process, the film composition changed significantly and full crystallization into $SrRuO_3$ could not proceed.

No conductivity was measured in the film consisting of seven spin cast layers during measurements with the digital multimeter. Conductance properties are believed to be severely affected at the grain boundaries of the $SrRuO_3$ crystallites. The fact that even seven spin cast layers did not form a conductive film proves that the goal could not be reached by this procedure.

Films were annealed at $500\,^{\circ}\mathrm{C}$ as well (not shown). A scratch was made on these film prior to the thermal treatment. No height differences were observed between the space between the islands and the scratch, indicating that no (significant) material had deposited between the islands. The widths of the islands were measured in the AFM image. The islands in Figure 5.11(a) were determined to have base widths of $0.7 \pm 0.3\ \mu\mathrm{m}$. The islands on the film annealed at $500\,^{\circ}\mathrm{C}$ showed considerable smaller islands of $0.3 \pm 0.2\ \mu\mathrm{m}$ ($R_{\mathrm{RMS}} = 28\ \mathrm{nm}$). The reason may be that crystallization events took place at lower temperatures on the film annealed at $500\,^{\circ}\mathrm{C}$. Consequent higher driving forces may have resulted in that more nucleation events had occurred. Another film was made at $500\,^{\circ}\mathrm{C}$, but with a heating rate of only $1\,^{\circ}\mathrm{C} \cdot \mathrm{min}^{-1}$ applied (not shown). The roughness of this film was higher than that prepared at $4\,^{\circ}\mathrm{C} \cdot \mathrm{min}^{-1}$ ($R_{\mathrm{RMS}} = 38\ \mathrm{nm}$).

5.2.2 Films on sapphire and platinum

Sapphire and platinum substrates were also used to form thin films on. Diffusion of Sr^{2+} will not proceed in these substrates, which was one of the reasons to study the film forming processes. The sapphire ($\alpha - Al_2O_3$) substrate (TBL-Kelpin) that was used was single crystalline, having the (001) plane at the surface. Platinum ($13\ \mathrm{nm}$) substrates were made on silicon wafers, coated with a ($100\ \mathrm{nm}$) titanium adhesion layer. The standard procedure was used to create films on these substrates.

AFM height images of a film on platinum and sapphire are presented in Figure 5.12 (a) and (b), respectively. The film height on platinum substrates varied significantly over the scanned area. The difference in height between the lowest parts and the highest parts of the film was nearly $150\ \mathrm{nm}$. No phases could be resolved from the XRD spectrum.

Films on sapphire had a relatively smooth layer from which parts protruded. Some of these protrusions showed sharp angles of 90° or 60°, indicating crystallinity. The features defined by angles of 90° (called plates) seemed to be in majority with respect to the pyramidal shaped protrusions.

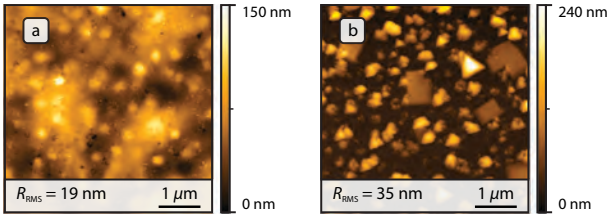

Figure 5.12: Tapping mode AFM height images of films deposited on platinum (a) and sapphire (b) substrates.

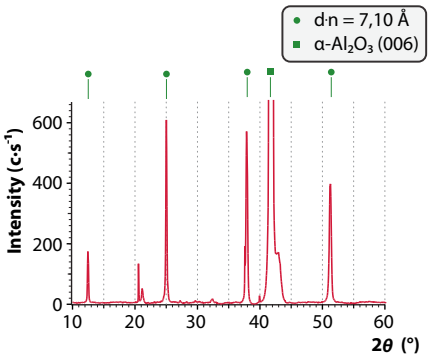

Figure 5.13: XRD spectrum of a film deposited on sapphire (001). ($\omega - 2\theta$ scan with a step size of 0.05°, measuring $40\ \mathrm{s} \cdot \mathrm{step}^{-1}$.)

Interestingly, the surface of these plates was aligned parallel to the substrate surface. This can not be explained by epitaxy, because the plates were randomly oriented.

An XRD $\omega - 2\theta$ scan of the film on sapphire contains a series of peaks that can all be described by $d \cdot n = 7.10$ Å (with n an integer). Note that this value is close to the $\vec{c}$-lattice constant of orthorhombic $SrRuO_3$. It might thus be that the plates consist of $SrRuO_3$. However, it is well conceivable that the plates consist of an other material, like strontium oxide (that has (101) planes that are separated by 3.49 Å.)

The films that had formed on both substrates are not of the desired quality. Both films have a roughness that is too high. Besides, the presence of $SrRuO_3$ forms a matter of debate. Nevertheless, these results show that film topography and crystallography can be controlled by the substrate.

5.2.3 Modifying oxidized silicon substrates

Diffusion of Sr^{2+} inside the oxidized silicon substrate is believed to change the stoichiometry of the film. One way – other than substituting the substrate – is to modify the substrate. In this context, a film of the strontium precursor solution was spin cast and annealed on an oxidized silicon substrate. The cations in this layer were expected to diffuse into the substrate and form a buffer against further diffusion of Sr^{2+}. Subsequently, precursor solution **1** was spin cast onto this substrate.

The buffer layer was characterized by tapping mode AFM (Figure 5.14) and was found very smooth. An XRD $\omega - 2\theta$ scan of the modified wafer revealed no peaks other than from silicon.

As can be seen from image 5.15(c), film roughening was limited after deposition of the SRO precursor solution. The corresponding optical microscopy images in (a) and (b) showed a remarkable result. On one edge of the films, circular patterns were observed that grew in quantity and coalesced in the direction of the opposite side.

In order to unveil the chemical composition of these patterns, XPS studies were performed on these dots and in regions between the dots. The results of this experiment are summarized in Table 5.1. The nature of the dotted structure could not be revealed by these studies. Regardless of the position on the film, no significant quantity of ruthenium was measured.

Circles of similar dimensions were observed on films that were cast on buffered substrates and annealed in two steps (not shown). The patterns were already visible after the first annealing step, that was conducted under either pure nitrogen or forming gas atmosphere. Different from the film annealed in a single step, the dots were randomly dispersed over the entire surface. AFM images of the films after the second annealing step did not show considerable differences with regard to the samples that were made accordingly on non-modified oxidized silicon substrates.

XPS measurements were conducted also on one of the films made by the two-step thermal treatment (see Table 5.1). Again, no significant compositional differences were observed between the dots and the layer in between the dots. No silicon was measured, indicating that this sample was – on average – thicker than that produced by the single-step thermal treatment. Ruthenium was detected in this case, which may be explained by the fact that the film had been exposed to the annealing temperature of $850\,^{\circ}\mathrm{C}$ for a shorter amount of time. No conductivity was measured in the film. Apparently, no $SrRuO_3$ thin films can be formed by this approach.

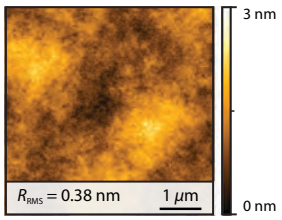

Figure 5.14: AFM height image of a buffer layer of strontium species on an oxidized silicon substrate.

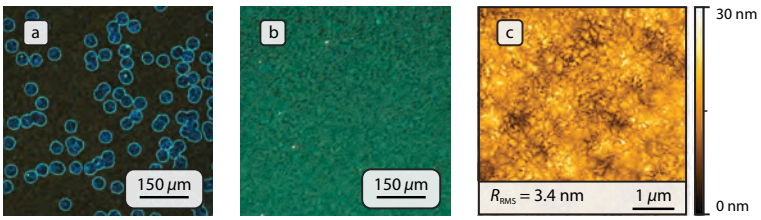

Figure 5.15: Dark field optical microscopy and tapping mode AFM height images of a film on an oxidized silicon substrate that was modified with strontium. The $5\times$ optical microscopy images in (a) and (b) were taken respectively on an edge and on the center of the film. The AFM scan that yielded image (c) was performed on a position at the center of the film.

Sample	Position scanned	O	Si	Ru	Sr
		atomic concentration (%)			
c	on a dot	65.2	24.0	0.07	10.8
c	between dots	64.5	22.7	0.07	12.5
d	on a dot	76.2	0.0	6.1	17.8
d	between dots	77.0	0.0	7.2	15.9

Table 5.1: Summary of XPS results for films that were coated on oxidized silicon substrates that had been enriched with strontium. Sample *c* was prepared by following the standard procedure. Sample *d* was prepared following the two-step method, of which the first step was performed in forming gas atmosphere at $500\,^{\circ}\mathrm{C}$ ($50\,^{\circ}\mathrm{C}\cdot\mathrm{h}^{-1}$). The second step was performed in a microwave furnace pre-heated to $850\,^{\circ}\mathrm{C}$ and kept at this temperature for 72 minutes.

5.3 Making changes to the solution

5.3.1 Using the alternative solutions

In Section 2.6, other solutions were described that could be used instead of the standard solution. Thin films were spin cast from these solutions in order to find out if the final topography can be controlled by the chemistry of the precursor solution.

AFM images of films made from the alternative precursor solutions are presented in Figure 5.16. Image (a), (b) and (c) were respectively measured on samples spin cast from solution **2a**, **2b**, and **3**. In the following, thin films made from the different solutions are not compared in high detail. The reason is that generally multiple variables are influenced by changes that are made to the solution. If for instance an other complex is used, solution properties like the pH, (thermal) stability, and viscosity may change.

Although the thin films do clearly differ from each other, the presence of protrusions on the surfaces is shared by all. Evidently, the formation of protrusions can therefore not simply be suppressed by achieving a better intermixing of the metal cations – as was attempted by application of solutions **2a** and **2b**.

The film produced from precursor solution **3** was found to have the lowest roughness. The concentration of precursor species in this solution was approximately one eight of that in solution **2a** and **2b**. This may explain why this film was more even than those prepared from the other solutions. Different attempts were made to increase the solubility of alternative Ru precursor complexes, but without success. Therefore, these complexes were unsuitable for polymer-assisted deposition.

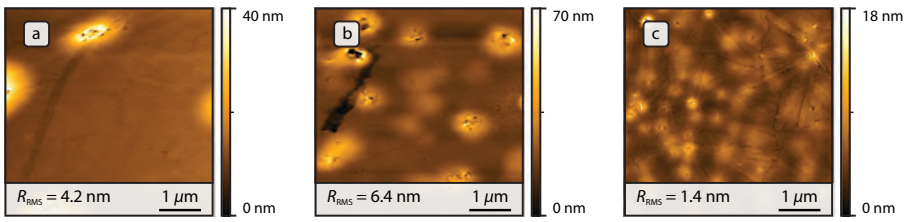

Figure 5.16: AFM images of films made with solution **2a** (a), **2b** (b), and **3** (c). (Because the concentration of precursor species in solution **3** was low, this solution was spin cast at $1500\ \mathrm{rpm}$ for one minute.)

5.3.2 Two approaches to change the solutions viscosity

The effect of changing the solution viscosity was studied by following two different approaches. In a first approach, solvent was evaporated in a vacuum oven at $50\,^{\circ}\mathrm{C}$ and approximately $100\ \mathrm{mbar}$. After some hours, the solution was retrieved from the oven and its viscosity was measured ($4.2\ \mathrm{mPa \cdot s}$). In a second approach, polyethyleneimine chains of different molecular weight (compared to those used in the standard solution) were used.

Selected images of the first and second approach are presented in Figure 5.17 and 5.18, respectively. After solvent removal, clearly larger protrusions were observed than in corresponding images made with a solution of lower viscosity (Figure 5.4). Also in the case that higher molecular weight polymeric species were used, larger protrusions were observed. This is believed to be related to the higher film thickness that is produced with solutions of higher viscosity.

The approaches that were evaluated in this chapter did not have the desired effect on the film forming processes. In no case, conductive thin films of $SrRuO_3$ had formed. Apparently, the film forming processes are complex and difficult to control.

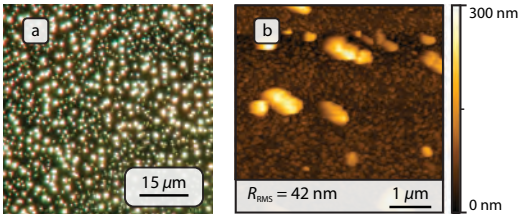

Figure 5.17: Optical microscopy (a) and tapping mode AFM height image (b) showing a film that was produced from a solution having a viscosity of $4.2\ \mathrm{mPa \cdot s}$. The film was made according to the same method that was used to produce the films in Figure 5.4.

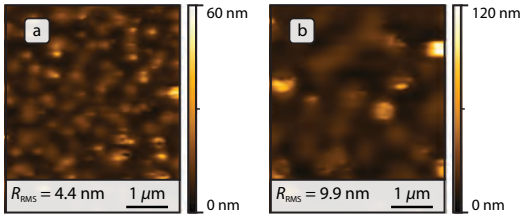

Figure 5.18: Contact mode AFM images of films made from solutions containing PEI molecules of $600\ \mathrm{g \cdot mol^{-1}}$ (a) and $50,000-100,000\ \mathrm{g \cdot mol^{-1}}$ (b). (Films were made according to the standard procedure, but with the hot plate temperature set at $120\,^{\circ}\mathrm{C}$ and $300\ \mu l$ solution added.)

Chapter 6

Conclusions and outlook

Conclusions

The formation of $SrRuO_3$ thin films on arbitrary substrates was not as favorable as was expected from considerations of the currently available literature on polymer-assisted deposition. Two possible causes may explain why no conducting $SrRuO_3$ thin films were formed during the attempts. The first possible cause can be found in the stability of the compound, of which ruthenium volatilizes already at a temperature of $850\,^{\circ}\mathrm{C}$. The second possible cause is related to the deposition method, that may (for most cases) require epitaxial substrates.

Protrusions were regularly observed on prepared films, and had developed during the thermal treatment. These protrusions are supposed to be the result of nucleation and growth of crystallites. Diffusion lengths inside the films are expected to be considerable during these processes, because the viscosity of the films will significantly decrease due to the decomposition processes. This property – that is supposed to contribute to the success of PAD for epitaxial growth processes – may be detrimental when films are formed on substrates that can not act as a template.

The marked topographical and compositional differences observed between films annealed at $600\,^{\circ}\mathrm{C}$ and $850\,^{\circ}\mathrm{C}$, is explained on the basis of the stability of $SrRuO_3$ crystallites. The protrusions that were observed after annealing at $600\,^{\circ}\mathrm{C}$ are believed to be $SrRuO_3$ crystallites. These protrusions were unstable at the high processing temperatures, which is expected to be related to the high curvature of the small crystallites. The different crystallization behavior between films produced from the standard procedure and multi-layer films may be explained by differences in the energy barriers of bulk and interface nucleation for $SrRuO_3$ and RuO_2, at the annealing temperatures applied.

Making changes to the film production procedure did not have the desired effects on the thin film quality (*i.e.* no conductive dense thin films, that were of appreciable roughness and contained crystalline $SrRuO_3$, were obtained). However, some changes clearly effected the final thin film microstructure. Compared to the standard procedure, smoother films were produced when *e.g.* annealing was applied in a confined space or when oxidized silicon substrates modified with Sr^{2+} were used. However, no presence of $SrRuO_3$ was detected in these layers and besides the films were insulating. The results of the various attempts illustrate the challenge of forming $SrRuO_3$ thin films on substrates that can not act as template during the deposition process.

Outlook

Since adaptations to the thermal treatment did not have the desired influence on the film forming processes, other possible measures should be further exploited. One such measure can be to take more effort to find alternative precursor complexes. If more stable complexes can be formed, release of the metal species may be delayed to higher temperatures, below which major organic decomposition processes have finished. The species are then supposed to be able to travel over shorter distances, and form crystallites that are flatter. The challenge of this approach should not be underestimated: finding and synthesis of new Ru and Sr precursor complexes that are extremely stable, soluble in the solvent system, and release the metals at analogous temperature, may be an impossible task.

Although thin films can not be obtained from the precursor solution, patterning of the solution is still an option. First results on patterning experiments proved that line patterns can be obtained from the standard solution. These preliminary results are a promising starting points for further research.

The formation of films on single crystalline substrates of desired lattice constants (*e.g.* YSZ (100)) may also be studied. According to the assumptions, smooth layers of good epitaxial quality can be produced on such substrates.

Bibliography

[1] R. J. Bouchard and J. L. Gillson. Electrical properties of $CaRuO_3$ and $SrRuO_3$ single crystals. *Mater. Res. Bull.*, 7(9):873–8, 1972.

[2] W. Bensch, H. W. Schmalle, and A. Reller. Structure and thermochemical reactivity of $CaRuO_3$ and $SrRuO_3$. *Solid State Ionics*, 43:171–7, 1990.

[3] X. D. Wu, S. R. Foltyn, R. C. Dye, Y. Coulter, and R. E. Muenchausen. Properties of epitaxial $SrRuO_3$ thin-films. *Appl. Phys. Lett.*, 62(19):2434–6, 1993.

[4] J. J. Randall and R. Ward. The preparation of some ternary oxides of the platinum metals. *J. Am. Chem. Soc.*, 81(11):2629–31, 1959.

[5] C. W. Jones, P. D. Battle, and P. Lightfoot. The structure of $SrRuO_3$ by time-of-flight neutron powder diffraction. *Acta Cryst.*, 45(3):365–7, 1989.

[6] W. Eysel and A. Geyer. PDF reference code: 43-0472. *ICDD Grant-in-Aid*, 1992.

[7] W. Chaisan, R. Yimnirun, S. Ananta, and D. P. Cann. Dielectric properties of solid solutions in the lead zirconate titanate-barium titanate system prepared by a modified mixed-oxide method. *Mater. Lett.*, 59(28):3732–7, 2005.

[8] R. Ramesh, A. Inam, W. K. Chan, B. Wilkens, K. Myers, K. Remschnig, D. L. Hart, and J. M. Tarascon. Epitaxial cuprates superconductor/ferroelectric heterostructures. *Science*, 252(5008):944–6, 1991.

[9] R. Ramesh, W. K. Chan, B. Wilkens, H. Gilchrist, T. Sands, J. M. Tarascon, and V. G. Keramidas. Fatigue and retention in ferroelectric Y-Ba-Cu-O/Pb-Zr-Ti-O/Y-Ba-Cu-O heterostructures. *Appl. Phys. Lett.*, 61(13):1537–9, 1992.

[10] J. F. Scott, C. A. Araujo, B. M. Melnick, and R. Zuleeg. Quantitative measurements of space-charge effects in lead zirconate-titanate memories. *J. Appl. Phys.*, 70(1):382–8, 1991.

[11] C. B. Eom, R. B. V. Dover, J. M. Phillips, D. J. Werder, J. H. Marshall, C. H. Chen, R. J. Cava, and R. M. Fleming. Fabrication and properties of epitaxial ferroelectric heterostructures with ($SrRuO_3$) isotropic metallic oxide electrodes. *Appl. Phys. Lett.*, 63(18):2570–2, 1993.

[12] S. Pöykkö and D. J. Chadi. Dipolar defect model for fatigue in ferroelectric perovskites. *Phys. Rev. Lett.*, 83(6):1231–4, 1999.

[13] Y. K. Wang, T. Y. Tseng, and P. Lin. Enhanced ferroelectric properties of $Pb(Zr_{0.53}Ti_{0.47})O_3$ thin films on $SrRuO_3/Ru/SiO_2/Si$ substrates. *Appl. Phys. Lett.*, 80(20):3790–2, 2002.

[14] J. P. Mercurio, J. H. Yi, M. Manier, and P. Thomas. Fabrication of $SrRuO_3$ powders and thin films by metalorganic decomposition. *J. Alloys Compd.*, 308(1-2):77–82, 2000.

[15] T. Kodaira, K. Nishio, I. Yamaguchi, S. Suzuki, K. Tsukada, and T. Tsuchiya. Synthesis and properties of highly conductive thin films as buffer layer from sol-gel process. *J. Sol-Gel Sci. Techn.*, 26(1-3):1049–53, 2003.

[16] H. Suzuki, Y. Miwa, H. Miyazaki, M. Takahashi, and T. Ota. Chemical solution deposition of conductive $SrRuO_3$ thin film on Si substrate. *Ceram. Int.*, 30(7):1357–60, 2004.

[17] R. Seveno, A. Braud, and H. W. Gundel. Elaboration of strontium ruthenium oxide thin films on metal substrates by chemical solution deposition. *Thin Solid Films*, 493(1-2):124–8, 2005.

[18] H. M. Luo, M. Jain, S. A. Baily, T. M. Mccleskey, A. K. Burrell, E. Bauer, R. F. DePaula, P. C. Dowden, L. Civale, and Q. X. Jia. Structural and ferromagnetic properties of epitaxial $SrRuO_3$ thin films obtained by polymer-assisted deposition. *J. Phys. Chem. B*, 111(26):7497–500, 2007.

[19] Q. X. Jia, T. M. McCleskey, A. K. Burrell, Y. Lin, G. E. Collis, H. Wang, A. D. Q. Li, and S. R. Foltyn. Polymer-assisted deposition of metal-oxide films. *Nat. Mater.*, 3(8):529–32, 2004.

[20] A. K. Burrell, T. M. Mccleskey, and Q. X. Jia. Polymer assisted deposition. *Chem. Commun.*, (11):1271–7, 2008.

[21] T. G. H. James. Gold technology in ancient egypt. *Gold Bull.*, 5(2):38–42, 1972.

[22] M. Ohring. *The Materials Science of Thin Films*, Academic Press, Hoboken, New Jersey, 1992.

[23] G. Cao. *Nanostructures and Nanomaterials - Synthesis, Properties and Applications*, Imperial College Press, London, 2004.

[24] U. Hasenkox, S. Hoffmann, and R. Waser. Influence of precursor chemistry on the formation of $MTiO_3$ (M = Ba, Sr) ceramic thin films. *J. Sol-Gel Sci. Techn.*, 12(2):67–79, 1998.

[25] R. W. Schwartz, T. Schneller, and R. Waser. Chemical solution deposition of electronic oxide films. *Cr. Chim.*, 7(5):433–61, 2004.

[26] J. C. W. Chien, B. M. Gong, J. M. Madsen, and R. B. Hallock. Polymer precursor synthesis and characterization of $YBa_2Cu_3O_{7-x}$. *Phys. Rev. B*, 38(16):11853–6, 1988.

[27] Y. Lin, J. S. Lee, H. Wang, Y. Li, S. R. Foltyn, Q. X. Jia, G. E. Collis, A. K. Burrell, and T. M. McCleskey. Structural and dielectric properties of epitaxial $Ba_{1-x}Sr_xTiO_3$ films grown on $LaAlO_3$ substrates by polymer-assisted deposition. *Appl. Phys. Lett.*, 85(21):5007–9, 2004.

[28] M. Jain, Y. Lin, P. Shukla, Y. Li, H. Wang, M. F. Hundley, A. K. Burrell, T. M. Mccleskey, S. R. Foltyn, and Q. X. Jia. Ferroic metal-oxide films grown by polymer assisted deposition. *Thin Solid Films*, 515(16):6411–5, 2007.

[29] M. A. Garcia, M. N. Ali, T. Parsons-Moss, P. D. Ashby, and H. Nitsche. Metal oxide films produced by polymer-assisted deposition (PAD) for nuclear science applications. *Thin Solid Films*, 516(18):6261–5, 2008.

[30] M. Jain, E. Bauer, F. Ronning, M. F. Hundley, L. Civale, H. Wang, B. Malorov, A. K. Burrell, T. M. McClesky, S. R. Foltyn, R. F. DePaula, and Q. Jia. Mixed-valence perovskite thin films by polymer-assisted deposition. *J. Am. Ceram. Soc.*, 91(6):1858–63, 2008.

[31] E. Bauer, A. H. Mueller, I. Usov, N. Suvorova, M. T. Janicke, G. L. N. Waterhouse, M. R. Waterland, Q. X. Jia, A. K. Burrell, and T. M. Mccleskey. Chemical solution route to conformal phosphor coatings on nanostructures. *Adv. Mater.*, 20(24):4704–7, 2008.

[32] R. Sun, M. Pu, G. Li, W. Wang, M. Pan, H. Zhang, M. Lei, W. Wu, X. Zhang, Y. Yang, Y. Zhang, and Y. Zhao. RE (RE = Sm, Eu, Gd)-doped CeO_2 single buffer layers for coated conductors prepared by chemical solution deposition. *Phys. Status Solidi A*, 206(7):1414–9, 2009.

[33] M. A. Garcia, M. N. Ali, N. N. Chang, T. Parsons-Moss, P. D. Ashby, J. M. Gates, L. Stavsetra, K. E. Gregorich, and H. Nitsche. Metal oxide targets produced by the polymer-assisted deposition method. *Nucl. Instrum. Methods Phys. Res., Sect. A*, 613(3):396–400, 2010.

[34] H. Luo, Y. Lin, H. Wang, C.-Y. Chou, N. A. Suvorova, M. E. Hawley, A. H. Mueller, F. Ronning, E. Bauer, A. K. Burrell, T. M. Mccleskey, and Q. X. Jia. Epitaxial GaN thin films prepared by polymer-assisted deposition. *J. Phys. Chem. C*, 112(51):20535–8, 2008.

[35] H. Luo, H. Wang, Z. Bi, G. Zou, T. M. Mccleskey, A. K. Burrell, E. Bauer, M. E. Hawley, Y. Wang, and Q. Jia. Highly conductive films of layered ternary transition-metal nitrides. *Angew. Chem. Int. Edit.*, 48(8):1490–3, 2009.

[36] H. Luo, Y. Lin, H. Wang, J. H. Lee, N. A. Suvorova, A. H. Mueller, A. K. Burrell, T. M. Mccleskey, E. Bauer, I. O. Usov, M. E. Hawley, T. G. Holesinger, and Q. X. Jia. A chemical solution approach to epitaxial metal nitride thin films. *Adv. Mater.*, 21(2):193–7, 2009.

[37] Y. R. Patta, D. E. Wesolowski, and M. J. Cima. Aqueous polymer–nitrate solution deposition of YBCO films. *Phys. C*, 469(4):129–34, 2009.

[38] M. Bhuiyan, M. Paranthaman, and K. Salama. Solution-derived textured oxide thin films—a review. *Supercond. Sci.*, 19(2):R1–21, 2006.

[39] R. P. Spiers, C. V. Subbaraman, and W. L. Wilkinson. Free coating of a Newtonian liquid onto a vertical surface. *Chem. Eng. Sci.*, 29(2):389–96, 1974.

[40] F. F. Lange. Chemical solution routes to single-crystal thin films. *Science*, 273(5277):903–9, 1996.

[41] P. Shukla, E. M. Minogue, T. M. McCleskey, Q. X. Jia, Y. Lin, P. Lu, and A. K. Burrell. Conformal coating of nanoscale features of microporous anodisc^{TM} membranes with zirconium and titanium oxides. *Chem. Commun.*, (8):847–9, 2006.

[42] A. K. Burrell, T. M. McCleskey, P. Shukla, H. Wang, T. Durakiewicz, D. P. Moore, C. G. Olson, J. J. Joyce, and Q. X. Jia. Controlling oxidation states in uranium oxides through epitaxial stabilization. *Adv. Mater.*, 19(21):3559–63, 2007.

[43] J. W. Steed, D. R. Turner, and K. J. Wallace. *Core concepts in supramolecular chemistry and nanochemistry*, John Wiley & Sons, Ltd., West Sussex, 2007.

[44] D. Cram. Preorganization – from solvents to spherands. *Angew. Chem., Int. Ed. Engl.*, 25(12):1039–57, 1986.

[45] G. L. Miessler and D. A. Tarr. *Inorganic Chemistry*, Pearson Education International, Minnesota, 2003.

[46] R. G. Pearson. Hard and soft acids and bases. *Chem. Br.*, 3:103–7, 1967.

[47] T. Kemmitt, L. G. Hubert-Pfalzgraf, G. J. Gainsford, and P. Richard. Cost efficient preparation of lead aminoalkoxides directly from lead (II) oxide. *Inorganic Chemistry Communications*, 8(12):1149–53, 2005.

[48] R. G. Pearson. Hard and soft acids and bases. *J. Am. Chem. Soc.*, 85(22):3533–9, 1963.

[49] T. R. Bhat and R. K. Iyer. Studies on EDTA complexes – VIII. *J. inorg. nucl. Chem.*, 29(1):179–85, 1967.

[50] Brewer science. Spin coater theory. http://www.brewerscience.com/research/processing-theory/spin-coater-theory/, (visited April 18, 2010).

[51] J. W. Cahn. Phase separation by spinodal decomposition in isotropic systems. *J. Chem. Phys.*, 42(1):93–99, 1965.

[52] A. Vrij and J. T. G. Overbeek. Rupture of thin liquid films due to spontaneous fluctuations in thickness. *J. Am. Chem. Soc.*, 90(12):3074–8, 1968.

[53] R. Xie, A. Karim, J. F. Douglas, C. C. Han, and R. A. Weiss. Spinodal dewetting of thin polymer films. *Phys. Rev. Lett.*, 81(6):1251–4, 1998.

[54] D. Grier and G. McCarthy. PDF reference code: 43-1027. *ICDD Grant-in-Aid*, 1991.

[55] J. H. Yi, P. Thomas, M. Manier, and J. P. Mercurio. Ruthenium oxide electrodes prepared by sol-gel spin-coating. *J. Phys. IV*, 8(P9):45–8, 1998.

[56] E. L. Bourhis. *Glass: Mechanics and Technology*, Wiley-VCH Verlag GmbH & Co. KGaA, Weinheim, Germany:1–366, 2007.

[57] S. H. Oh and C. G. Park. Nanoscale characterization of interfacial reactions in $SrRuO_3$ thin film on Si substrate. *Surf. Interface Anal.*, 31(8):796–798, 2001.

[58] P. F. Campbell, M. H. Ortner, and C. J. Anderson. Differential thermal analysis and thermogravimetric analysis of fission product oxides and nitrates to $1500\,^{\circ}\mathrm{C}$. *Anal. Chem.*, 33(1):58–61, 1961.

[59] M. Hiratani, Y. Matsui, K. Imagawa, and S. Kimura. Hydrogen reduction properties of RuO_2 electrodes. *Jpn. J. Appl. Phys. 2*, 38(11A):L1275–7, 1999.

[60] Pfoertsch and McCarthy. PDF reference code: 30-1468. *ICDD Grant-in-Aid*, 1977.

[61] S. Y. Hou, J. Kwo, R. K. Watts, J. Y. Cheng, and D. K. Fork. Structure and properties of epitaxial $Ba_{0.5}Sr_{0.5}TiO_3/SrRuO_3/ZrO_2$ heterostructure on Si grown by off-axis sputtering. *Appl. Phys. Lett.*, 67(10):1387–9, 1995.

[62] H. N. Lee, D. Zakharov, S. Senz, A. Pignolet, and D. Hesse. Growth and characterization of non-*c*-axis-oriented $SrBi_2Ta_2O_9$ epitaxial thin films on Si(100) substrates with $SrRuO_3$ bottom electrodes. *Integr. Ferroelectr.*, 39(1-4):73–80, 2001.

[63] S. K. Tyrlik, K. Kurzak, and S. L. Randzio. Reactions of commercial ruthenium chlorides with O-donor ligands – reactions with water – UV-Vis investigation of soluble products – analysis, thermogravimetry and an IR study of precipitated solids. *Transition Met. Chem.*, 20(4):330–7, 1995.

[64] A. R. Oki and R. J. Morgan. An efficient preparation of 4,4'-dicarboxy-2,2'-bipyridine. *Synthetic Commun.*, 25(24):4093–7, 1995.

[65] M. K. Nazeeruddin and M. Grätzel. Ch. 27, an improved synthesis of *cis*-dithiocyanato-bis(4,4'-dicarboxy-2,2'-bpy)Ru(II) sensitizers. *Inorganic Syntheses, Vol. 33*, John Wiley & Sons, Inc.:185–9, 2004.

[66] M. K. Nazeeruddin, K. Kalyanasundaram, and M. Grätzel. Ch. 31, a one-pot synthesis of tetrahydronium tris(4,4'-dicarboxylato-2,2'-bipyridine)-ruthenium(II) dihydrate. *Inorganic Syntheses, Vol. 32*, John Wiley & Sons, Inc.:181–5, 1998.

Appendix A

Synthesis procedures for alternative precursor solutions

A.1 Intermixing Sr(II) and Ru(III) species (solution 2)

Approach 1 A ruthenium precursor solution was made according to the procedure described on page 13. One adaptation was made to this procedure: the amount of added $RuCl_3 \cdot 3\,H_2O$ was halved. $224\ \mathrm{mg}$ $(0.76\ \mathrm{mmol})$ EDTA was added to this solution after which vigorous stirring was continued for twenty minutes. $160\ \mathrm{mg}$ $(0.75\ \mathrm{mmol})$ $Sr(NO_3)_2$ was subsequently added and the resulting solution was moderately stirred for three days.

After these days the dark brown solution still contained fine dispersed solids. A $25\,\%\ w/w$ aqueous ammonium hydroxide solution was added to the solution until a pH of 4.3 was reached. The solution was additionally stirred for 24 hours.

Approach 2

A solution of $500\ \mathrm{mg}$ branched PEI $(10,000\ \mathrm{g \cdot mol^{-1}})$ in $2.5\ \mathrm{ml}$ water was prepared. After $224\ \mathrm{mg}$ $(0.76\ \mathrm{mmol})$ EDTA had completely dissolved in this solution, $160\ \mathrm{mg}$ $(0.75\ \mathrm{mmol})$ $Sr(NO_3)_2$ was added. The solution was stirred for 30 minutes. The acidity of this solution was adjusted by adding $37\,\%\ w/w$ hydrochloric acid until pH fell just below 5.

A solution of $196\ \mathrm{mg}$ $(0.75\ \mathrm{mmol})$ $RuCl_3 \cdot 3\,H_2O$ in $2.5\ \mathrm{ml}$ water was prepared twenty hours before. Meanwhile it had been stirred moderately. Within this timeframe, soluble oligomers are thought to form due to hydrolysis with water molecules.[63] Aging of the $RuCl_3$ solution was essential to inhibit precipitation upon addition to the polymeric solution. The solution was added in drops to the other solution in approximately fifteen minutes.

A.2 Supramolecular solutions of PEI and tris-(4,4'-dicarboxy-2,2'-bipyridine)-ruthenium(II) complexes (solution 3)

Synthesis of 4,4'-dicarboxy-2,2'-bipyridine In a $50\ \mathrm{ml}$ three-necked round-bottomed flask containing a magnetic stir bar, $45\ \mathrm{ml}$ sulphuric acid $(96\,\%)$ were added. The flask was heated in an oil bath to $70\,^{\circ}\mathrm{C}$ while stirring the solvent at $\sim 500\ \mathrm{rpm}$.

An amount of $2.0\ \mathrm{g}$ $(10.7\ \mathrm{mmol})$ 4,4'-dimethyl-2,2'-bipyridine was added and stirring speed was increased to $\sim 1000\ \mathrm{rpm}$. Without external heating, $9.6\ \mathrm{g}$ $(32.3\ \mathrm{mmol})$ potassium dichromate was

added in small portions during 30 minutes. The temperature was kept between 65 and $90\,^{\circ}\mathrm{C}$; cooling was applied when the reaction temperature exceeded $80\,^{\circ}\mathrm{C}$. After all potassium dichromate was added, vigorous stirring of the mixture was continued until its temperature reached $40\,^{\circ}\mathrm{C}$.

The deep green solution was poured over $300\ \mathrm{ml}$ ice water with additional external cooling. This mixture was filtered by vacuum filtration using quantitative filter paper (Whatman; particle retention $2.7\ \mu\mathrm{m}$). The residue was washed with water until the water was no longer discolored. The resulting light yellow solid was further purified by refluxing it in $70\ \mathrm{ml}$ nitric acid ($65\,\%$) at $124\,^{\circ}\mathrm{C}$ for 4 hours.

The solution was poured over ice, diluted with $400\ \mathrm{ml}$ water and cooled to $5\,^{\circ}\mathrm{C}$. The precipitate was filtered by vacuum filtration through quantitative filter paper (Whatman; particle retention $7\ \mu\mathrm{m}$) and washed with $5 \times 20\ \mathrm{ml}$ water and then with $2 \times 10\ \mathrm{ml}$ acetone. The solid was collected on a petri dish, covered, and placed in an oven heated to $90\,^{\circ}\mathrm{C}$. The solid was allowed to dry overnight after which it was ground. The resulting fine white powder ($2.2\ \mathrm{g}$, $84\,\%$) was stored in a $10\ \mathrm{ml}$ screw cap vial. This procedure is based on one proposed by Oki and co-workers.[64]

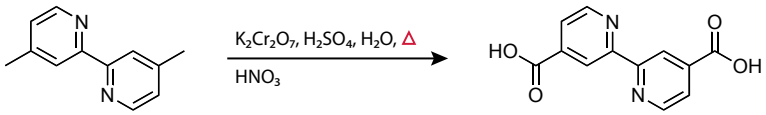

Figure A.1: Synthesis of 4,4'-dicarboxy-2,2'-bipyridine from 4,4'-dimethyl-2,2'-bipyridine.

Synthesis of tris-(4,4′-dicarboxy-2,2′-bipyridine)-ruthenium(II)dihydrate ($RuLL_3 \cdot 2\,H_2O$)

An amount of $30\ \mathrm{ml}$ reagent grade N,N'-dimethylformamide (DMF) was added to a $250\ \mathrm{ml}$ three-necked round-bottomed flask fitted with a reflux condenser, magnetic stir bar and gas inlet. From this point, the flask was continuously flushed with a small flow of nitrogen gas.

$261\ \mathrm{mg}$ ($1.0\ \mathrm{mmol}$) $RuCl_3 \cdot 3\,H_2O$ was dissolved while stirring at $\sim 500\ \mathrm{rpm}$. After 15 minutes of stirring, another $30\ \mathrm{ml}$ of DMF was added. The flask was completely wrapped in aluminum foil to prevent possible trans isomerization of the bis-complex.[65] Trans isomerization of the bis-complex will inhibit the formation of the tris-complex.

An amount of $879\ \mathrm{mg}$ ($3.6\ \mathrm{mmol}$) 4,4'-dicarboxy-2,2'-bipyridine was added to the solution and the stirring speed was increased to $1000\ \mathrm{rpm}$. The flask was immersed in an oil bath of $180\,^{\circ}\mathrm{C}$. Aliquots of the reaction mixture were transferred to a 110-QS quartz cuvette (Hellma), diluted with ethanol and analyzed with a Cary 50 UV/Vis spectroscope (Varian). After 5 hours, the spectrum showed maxima at $567\ \mathrm{nm}$, $411\ \mathrm{nm}$ and $317\ \mathrm{nm}$ having relative intensities of $1{:}1.18{:}2.81$. These values lie close to those reported for the bis-complex.[65] To obtain the tris-complex, $12\ \mathrm{ml}$ of a $0.5\ \mathrm{M}$ aqueous sodium hydroxide solution was added. Deprotonation of the carboxyl groups occur, yielding more basic ligands. Refluxing was continued for 15 hours.

The oil bath was removed and the reaction mixture was allowed to cool for 1 hour without additional cooling. Vigorous stirring was maintained during this process. The solution was concentrated to $\sim 20\ \mathrm{ml}$ by placing the flask in a vacuum drying oven (Binder) pre-heated to $110\,^{\circ}\mathrm{C}$. The pressure inside the oven was reduced to $200\ \mathrm{mbar}$. After 2 hours, the temperature was increased to $120\,^{\circ}\mathrm{C}$ and pressure was reduced to $10\ \mathrm{mbar}$.

The solution was cooled to room temperature and filtered on a sintered glass crucible. The dark orange filtrate was washed five times with $10\ \mathrm{ml}$ DMF and two times with $4\ \mathrm{ml}$ diethyl ether. The solid was placed in an Erlenmeyer flask and recrystallized from $\sim 100\ \mathrm{ml}$ diethyl ether and $\sim 100\ \mathrm{ml}$ methanol. This solution was filtered using a sintered glass funnel. The filtrate was collected on a Petri dish, covered, and placed on a hot plate set to $100\,^{\circ}\mathrm{C}$. The solid was allowed to dry for 2 hours ($0.86\ \mathrm{g}$).

The solid was placed in a $100\ \mathrm{ml}$ flask containing $90\ \mathrm{ml}$ water. To remove unreacted ligands, the solution was filtered through a glass funnel containing a quantitative filter paper (Whatman; particle retention $7\ \mu\mathrm{m}$). The residue was collected in a $250\ \mathrm{ml}$ round-bottomed flask and pH of this solution was taken to 2.5 by addition of a $0.1\ \mathrm{M}$ hydrochloric acid solution. The solution was vigorously mixed by swirling the flask for 2 minutes. The flask was subsequently allowed to stand for 20 hours at $1\,^{\circ}\mathrm{C}$, during which precipitation took place.

A pasteur pipette was used to remove the light yellow aqueous solution, leaving the dark orange sediment inside the flask. The content of the flask was subsequently filtered by vacuum filtration using HA-type filter paper (Millipore; particle retention $0.45\ \mu\mathrm{m}$). The residue was rinsed with $5 \times 1.5\ \mathrm{ml}$ aqueous hydrochloric acid with a pH of 2.5. The resulting clay-like solid was collected on a Petri dish, covered, and placed on a hot plate set at $100\,^{\circ}\mathrm{C}$. After 3 hours, the solid was ground and collected in a $5\ \mathrm{ml}$ screw cap vial ($0.559\ \mathrm{mg}$, $64\,\%$). The procedure is based on one proposed by Nazeeruddin *et al.*[66]

Synthesis of the SRO precursor solution

A quantity of $82\ \mathrm{mg}$ $RuLL_3 \cdot 2\,H_2O$ was dissolved in a mixture of $600\ \mu\mathrm{l}$ water and $100\ \mu\mathrm{l}$ $25\,\%\ w/w$ aqueous ammonium hydroxide solution. An amount of $57\ \mathrm{mg}$ branched PEI ($10,000\ \mathrm{g \cdot mol^{-1}}$) was added and stirred for one hour. $312\ \mu\mathrm{l}$ strontium precursor solution – made following the procedure on page 13 – were added. The resulting solution was stirred moderately for one hour. Before spin casting this solution, it was filtered through an FP 30/0.8 CA filter unit (Whatman; particle retention $0.8\ \mu\mathrm{m}$).

A.3 Blocking Ru co-ordinating sites with 2,2′-bipyridine (solution 4)

A quantity of $30\ \mathrm{ml}$ reagent grade N,N'-dimethylformamide was added to a $250\ \mathrm{ml}$ round-bottom flask equipped with a reflux condenser, magnetic stir bar and nitrogen gas inlet. The solvent was continuously stirred and flushed with a gentle N_2 stream. $261\ \mathrm{mg}$ $RuCl_3 \cdot 3\,H_2O$ ($1.0\ \mathrm{mmol}$) were dissolved while stirring at $\sim 550\ \mathrm{rpm}$. After fifteen minutes, another amount of $30\ \mathrm{ml}$ DMF was added.

To this solution, $167\ \mathrm{mg}$ 2,2'-bipyridine ($1.05\ \mathrm{mmol}$) were added and the stirring speed was doubled. The flask was immersed in an oil bath set to $180\,^{\circ}\mathrm{C}$. The mixture was refluxed for three hours after which a dark purple solution was obtained. It was subsequently allowed to cool to room temperature by removing the oil bath and without external cooling. The solvent was extracted in a rotary evaporator, after which the solid was collected and stored without further purification.

An aliquot of $23\ \mathrm{mg}$ of the solid was added to a solution of $500\ \mathrm{mg}$ PEI in $2.5\ \mathrm{ml}$ water. The solution turned peach-orange after seconds, but even after two days the solid had not completely dissolved.


UNIVERSITY OF TWENTE.
MESA+
INSTITUTE FOR NANOTECHNOLOGY